

Stress-driven nonlinear dynamics of ion-induced surface nanopatternsJ. Muñoz-García ^{1,*}, R. Cuerno ¹ and Mario Castro ^{2,3}¹*Departamento de Matemáticas and Grupo Interdisciplinar de Sistemas Complejos (GISC), Universidad Carlos III de Madrid, 28911 Leganés, Spain*²*GISC and Grupo de Dinámica No Lineal (DNL), Escuela Técnica Superior de Ingeniería (ICAI), Universidad Pontificia Comillas, 28015 Madrid, Spain*³*School of Mathematics, University of Leeds, Leeds LS2 9JT, United Kingdom* (Received 7 September 2018; revised manuscript received 20 September 2019; published 21 November 2019)

For many solid targets, like semiconductors, that become amorphous under irradiation by energetic ions, the outermost surface layer displays formation of asymmetric nanoscale ripples in macroscopic timescales. In contrast to the well-known macroscopic case of an incompressible thin fluid film spreading down an incline, in which the morphological instability is controlled by gravity, here we prove that residual stress induced by the ions is responsible for pattern formation and accounts for its long-time dynamics, even in absence of sputtering effects. Using a continuum framework, we derive closed nonlinear evolution equations for the depth of the irradiated layer. This description includes novel terms associated with the spatial distribution of damage that builds up through sustained bombardment, thus extending to the nanoscale classic models of macroscopic fluid-flow systems, and providing detailed information on the pressure and velocity fields within the irradiated layer. Numerical simulations reproduce the main dynamical features of surface nanopatterning under the assumed conditions, elucidating the ensuing nonlinear properties on ripple amplification and transport.

DOI: [10.1103/PhysRevB.100.205421](https://doi.org/10.1103/PhysRevB.100.205421)**I. INTRODUCTION**

Nonlinear effects are well known to control the large-scale properties of spatially extended systems far from equilibrium [1]. For example, for pattern-forming systems, in which the selection of a typical scale can be described (via the interplay between stabilizing and destabilizing mechanisms) within linear approximation of perturbations around the homogeneous state [2], the system behavior is ultimately dictated by the nonlinear effects triggered by perturbations themselves. Essential pattern properties influencing their practical use, like, e.g., stability with respect to secondary instabilities, detailed space structure, and other, crucially depend on nonlinear interactions [3].

Historically, important instances for pattern formation have included hydrodynamic instabilities in macroscopic fluid-flow systems [4]. Nowadays, nanoscience is showcasing a host of systems and processes with novel pattern-forming properties [5], and also analogies of macroscopic behavior. Recent examples include the classic Rayleigh-Taylor instability being reproduced by nanodot formation via laser melting of Au thin films [6], or soft-matter-like surface wrinkles being induced at nanoscales by ion bombardment [7]. Precisely, ion-beam sputtering (IBS) stands out as the particularly versatile nanopatterning technique which prompted Taniguchi to coining the term “nanotechnology” in the early 70’s [8]. It consists in irradiating a solid target with a broad ion beam impinging under a well-defined incidence angle θ to the surface normal [9,10]; this erodes material out, surprisingly inducing nanoscale surface ripples, as experimentally found quite early on [11,12].

To date, these nanopatterns have found a large number of applications for, e.g., optoelectronics [13,14], photovoltaics [15], nanolithography [16,17], biomedicine [18,19], or the synthesis of novel structures [20] and materials [21], holding potential for many other [7].

For low-to-medium ion energies E , roughly between 0.5 and 100 keV, semiconductors and other materials become amorphized by IBS [22]. An ultrathin, highly viscous amorphous layer is produced and maintained under irradiation on top of an unirradiated bulk. In line with recent results for, e.g., quartz, according to which ion-irradiated materials are more similar to fluids than to amorphous phases [23], a model based on the flow of the irradiated layer, within linear approximation [24], has shown how the dynamics of such layer controls key morphological properties of the surface seen in experiments.

Although the linear stages of evolution of IBS nanopatterns have thus been understood, nonlinear properties including their stabilization, ordering, and in-plane transport, have remained theoretically elusive, see, e.g., Ref. [25] for a recent review. Indeed, nonlinear descriptions of IBS surface nanopatterning are available [26–30], but they assume erosion (sputtering) as the main cause for the surface instability, which implies for instance that pattern formation can occur for any value of the incidence angle including $\theta = 0^\circ$, contradicting recent experimental observations [25]. The limitations to the predictive power of such nonlinear descriptions are underscored by yet more recent experiments on Si with Ar⁺ ions for very low E at which the sputtering yield is negligible [31], which find a pattern formation process just like the one seen at higher E and erosion rates [24,25,32].

However, assuming viscous flow as the main relaxation mechanism, the source of nonlinear behavior in IBS

*jamunoz@math.uc3m.es

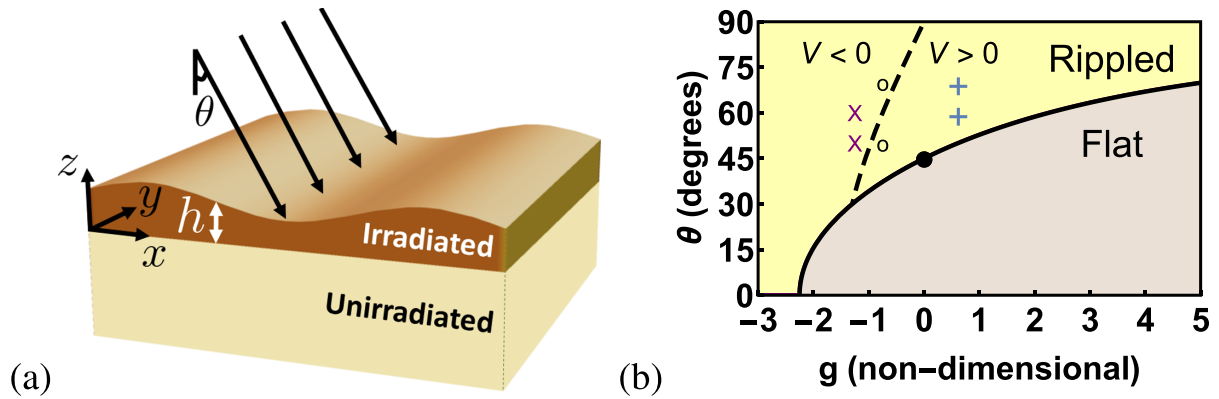


FIG. 1. (a) Sketch of the physical system. Ions arrive under incidence angle θ . (b) Morphological diagram in terms of θ and the stress ratio g defined in Eq. (6). Ripples (respectively, do not) form for $\theta > \theta_c$ (respectively, $\theta < \theta_c$) throughout the lighter (respectively, darker) shaded area. The solid line provides the critical angle for pattern formation θ_c as a function of g , as predicted by Eq. (7), with $\theta_c = 0^\circ$ for $g \leq -2.25$. Symbols \times , $+$, and \circ indicate conditions for the representative numerical simulations defined in Table I. The symbol \bullet highlights the fact that $\theta_c(g = 0) = 45^\circ$. Within the rippled phase, the dashed line separates regions in which the (linear) velocity of ripple motion V is negative (left of the line) or positive (right of the line) according to Eq. (13).

surface nanopatterning is not apparent either. Indeed, in general nanosystems present conspicuous challenges to direct replication of classic hydrodynamical instabilities. Leaving aside the potential breakdown of continuum approaches like the Navier-Stokes equation at sufficiently small scales [33], additional difficulties exist. For instance, both gravity and fluid inertia are expected to be irrelevant at the nanoscale, since the Reynolds number unavoidably becomes small [34,35], rendering inoperative the basic mechanisms controlling pattern formation in, e.g., the analogous classic problem of a macroscopic fluid layer flowing down an inclined plane (at angle θ) [4,36]. Hence, the physical origin of the nonlinearities expected to control the long-time properties of pattern formation [2] is not obvious in nanometric systems. In particular, convective nonlinear effects associated with inertia are absent for IBS.

In this paper, we elucidate the nonlinear effects that control the large-scale evolution of IBS surface nanopatterns for amorphizable targets close to pattern onset, as emerging from the interplay between the space distribution of residual stress induced by sustained bombardment, and its subsequent relaxation via highly viscous flow. While we focus on the case of IBS systems with a negligible sputtering rate [31], we expect our results to apply to more general cases, sufficiently close to onset of the pattern formation instability. Specifically, we implement a lubrication approximation [36,37] of a continuum flow model to obtain a strongly nonlinear time evolution equation for the thickness of the irradiated layer. Closely related models display a plethora of fascinating, nontrivial nonlinear properties, like, e.g., localized structures and solitonlike behavior [36,38,39], which may thus prove of relevance also in the nanoscale IBS context. Our theory reveals nontrivial correlations between dynamic and morphological properties of the patterns which are robust to nonlinear effects and are susceptible of experimental verification. This would further confirm viscous flow driven by ion-induced stress as a crucial contribution to the nonlinear dynamics of IBS surface nanostructuring, not only under negligible sputtering conditions [31] but also at higher energies and erosion rates [24,25,32].

This paper is organized as follows. Section II contains the presentation and derivation of our continuum model, many details of which are left to Appendices A through C. Section III presents analytical predictions which can be derived from the model within a linear approximation. A more complete study needs to address nonlinear properties and is carried out numerically in Sec. IV which, after considering the informative case of one-dimensional (1D) systems, also deals with the full 2D dynamics of the irradiated layer. Finally, Sec. V summarizes the main results of our work, and states our conclusions and outlook on future developments.

II. THEORETICAL DESCRIPTION

Under standard low-to-medium E conditions for IBS, impinging ions lose their kinetic energy through a series of binary collisions inside the solid [9]. For a typical ion flux of $10 \text{ ion nm}^{-2} \text{ s}^{-1}$ or smaller, this amorphizes a surface layer atop an underlying pristine (*unirradiated*) target [see a sketch in Fig. 1(a)], with a density and depth (a few nm, of the order of the ion range) which stabilize after a few seconds of irradiation [25,40,41]. The structural disorder in the irradiated layer makes it more similar to a highly viscous fluid than to an amorphous phase of the same material [23]. In particular, experimental estimates for noble-gas irradiation of Si conclude [32,42] that the viscosity μ of this layer is very high, close to 1 GPa min, while assuming viscoelastic-like constitutive laws between strain and stress, which are more complex than that for a simple Newtonian fluid, does not improve predictive power in our experimental context [32,43]. Thus the effect of the irradiation can be expressed as residual stress (*forcing*) that is relaxed via Newtonian viscous flow (*relaxation*) [44–46] and which, as experimentally assessed [47], does not depend on the initial structural state (e.g., crystalline or amorphous) of the target. Results from molecular dynamics (MD) simulations indicate [24] that the corresponding stress tensor is traceless, so that the irradiated layer is incompressible.

TABLE I. Parameter values employed in our numerical simulations, as obtained from Eq. (2), for $G_s = 0.4$ GPa, $\sigma = 10$ GPa nm, $\mu = 0.83$ GPa min with $G_b = -0.1$ GPa nm⁻¹ implying $g = g_1 = -1.25$ [x symbols in Fig. 1(b)], $G_b = 0.05$ GPa nm⁻¹ implying $g = g_2 = 0.625$ [+ symbols in Fig. 1(b)], and $G_b = -0.06$ GPa nm⁻¹ implying $g = g_3 = -0.75$ [o symbols in Fig. 1(b)]. Incidence angles θ as indicated.

Coefficient	$g = g_1, \theta = 50^\circ$	$g = g_1, \theta = 60^\circ$	$g = g_2, \theta = 60^\circ$	$g = g_2, \theta = 70^\circ$	$g = g_3, \theta = 50^\circ$	$g = g_3, \theta = 70^\circ$	Physical units
a_1	0.71	0.62	0.63	0.46	0.71	0.46	1/min
a_2	-0.18	-0.21	0.10	0.11	-0.11	-0.14	1/(nm min)
b_1	-0.12	-0.36	-0.36	-0.55	-0.13	-0.55	1/min
b_2	0.30	0.18	0.18	0.08	0.30	0.08	1/min
c	-0.05	-0.04	0.02	0.01	-0.02	-0.01	1/(nm min)
γ	4	4	4	4	4	4	nm/min
Name	(a)	(b)	(c)	(d)	(e)	(f)	

Hence, we formulate a flow model in which we assume $\nabla \cdot \mathbf{v} = 0$ (fluid incompressibility), where $\mathbf{v}(\mathbf{r}, t) = (u, v, w)$ is the fluid velocity at point $\mathbf{r} = (x, y, z)$ in the irradiated layer and time t , momentum conservation for this highly viscous layer [32,42] reducing to [4,36] $\nabla \cdot \mathbf{T} = \mathbf{0}$, where inertial terms are dropped and the stress tensor $\mathbf{T} = \mathbf{T}^F + \mathbf{T}^{\text{ext}}$ is the sum of the fluidic term $\mathbf{T}^F = -p\mathbb{I} + \mu(\nabla\mathbf{v} + \nabla\mathbf{v}^T)$ and an external contribution \mathbf{T}^{ext} due to the irradiation. Here, $p(\mathbf{r}, t)$ is hydrostatic pressure, μ is viscosity, and \mathbb{I} is the identity tensor. MD results additionally indicate [24,41,47] that the residual stress is nonhomogeneously distributed in the irradiated layer and that its value \mathbf{T}^{ext} , for a target bombarded under an oblique incidence angle θ is well approximated by a θ rotation of the stress distribution generated under normal incidence [24]. Still, very little additional information is available on the detailed space variation of \mathbf{T}^{ext} . In order to make analytical progress, we will simplify such a space variation and assume it to occur only along the ion-beam direction and with a constant (*bulk*) gradient G_b (see Appendix A for details). Remarkably, very recent MD simulations [48] of Ar⁺ irradiation of Si for $E = 30$ eV (under which the sputtering yield is negligible [31]) seem consistent with such a simple variation for \mathbf{T}^{ext} . Combined with the previous assumption on θ dependence, this implies $\nabla \cdot \mathbf{T}^{\text{ext}} = (2G_b \sin \theta, 0, -2G_b \cos \theta)$, see Appendix A.

Thus far, the fluid-flow model just proposed generalizes to 2D substrates the one put forward in Ref. [24] for 1D substrates. To complete the description, the previous conservation and constitutive laws have to be supplemented with boundary conditions. Although more elaborate conditions can be considered [24], in view of the present stage of development, and as a compromise between mathematical simplicity and predictive power, we assume the interface between the irradiated layer and the unirradiated bulk to be flat, without slip or fluid penetration. If pattern formation onset is dominated by redistributive rather than by sputtering effects [25,31], the latter can be neglected. At the free surface [$z = h(x, y, t)$, see Fig. 1(a)] simple stress-balance and kinematic conditions are imposed, i.e., $\mathbf{T} \cdot \hat{\mathbf{n}} = 2\sigma\kappa\hat{\mathbf{n}}$ and $Dz/Dt = w$, respectively, where σ is surface tension, κ is curvature, $\hat{\mathbf{n}}$ is the exterior unit normal, and D/Dt is the total or convective time derivative [36,37,49]. While our present boundary condition at the irradiated/unirradiated (i/u) interface is simplified, the advantage is that we can now make further analytical progress, which was hampered in Ref. [24] and remained limited to linear approximations.

The present model, although being conspicuously free from inertial terms, is still highly nonlinear. In order to simplify it, we perform a gradient expansion similar to the classical long-wave theory of falling films for low flow rates [4,36]. This will allow us to derive a single nonlinear evolution equation for h , which captures the nontrivial morphological dynamics both, for short irradiation times in which linear approximations are accurate, and well into the nonlinear regime. Specifically, our next step is to consider $\sigma = \alpha\epsilon^{-2}$, where α is an arbitrary proportionality constant and ϵ is dimensionless and small. At this, we anticipate that the typical pattern wavelength scales with $\sigma^{1/2}$, as in the linear stability analysis of related, experimentally validated, IBS models [24,44–46]. Then, we introduce slow scales $X = \epsilon x$, $Y = \epsilon y$, and $T = \epsilon t$, and perform a series expansion of \mathbf{v} and p in powers of ϵ to obtain a closed nonlinear evolution equation for h ; see Appendix A for details. To order ϵ^2 , using the original coordinates and the corresponding subscripts to denote the partial derivatives, this reads

$$h_t = -a_1 h h_x - a_2 h^2 h_x + \nabla \cdot (h^2 \mathbf{B} \cdot \nabla h) + c \nabla \cdot (h^3 \nabla h) - \gamma \nabla \cdot (h^3 \nabla \nabla^2 h), \quad (1)$$

where the coefficients are

$$a_1 = \frac{3G_s \sin(2\theta)}{2\mu}, \quad a_2 = \frac{2G_b \sin(\theta)}{\mu}, \quad \gamma = \frac{\sigma}{3\mu},$$

$$\mathbf{B} = \begin{bmatrix} \frac{3G_s \cos(2\theta)}{2\mu} & 0 \\ 0 & \frac{3G_s \cos^2(\theta)}{2\mu} \end{bmatrix}, \quad c = \frac{2G_b \cos(\theta)}{3\mu}, \quad (2)$$

and G_s is the value of the ion-induced stress at the free surface, up to numerical constants, see Eq. (A16). Consistent with the neglect of sputtering, Eq. (1) conserves the total mass of the irradiated layer, reading as $h_t = -\nabla \cdot \mathbf{J}$ with $\mathbf{J} = (a_1 h^2/2 + a_2 h^3/3, 0) - (h^2 \mathbf{B} + c h^3 \mathbb{I}) \cdot \nabla h + \gamma h^3 \nabla \nabla^2 h$. All terms on the right-hand-side of Eq. (1) are nonlinear, this equation providing the IBS analog of the classic Benney equation for a macroscopic fluid film down an incline [4,36]. Such as they appear in the conserved surface current \mathbf{J} , they correspond, respectively, to Burgers-like terms reflecting a non-null streamwise component of the external driving, the anisotropic cross-stream component of the latter, and the classic contribution of surface tension to viscous film spreading [37,49,50]. The precise form of the Benney equation for a macroscopic fluid flowing down an inclined plane can be

retrieved from (the one-dimensional version of) Eq. (1) by replacing $a_1 \rightarrow 0$ and $h^2\mathbf{B} \rightarrow h^6\mathbb{I}$.

Likewise, the particular $\mathbf{B} = \mathbf{0}$ case of Eq. (1) happens to also describe, within a lubrication approximation, the dynamics of another macroscopic system with fluid thicknesses between two and three orders of magnitude larger than the ones we are presently considering. Specifically, that of a viscous film destabilized by a surface tension gradient induced by an external temperature field, which is opposed by a stabilizing gravitational force [51,52]. Besides lacking the \mathbf{B} term, the only difference between the evolution equation considered in Refs. [51,52] and Eq. (1) is that, in the former, $a_2 < 0$ and $c > 0$ have fixed signs imposed by the stabilizing role of gravity, while in our case both c and a_2 take the sign of G_b , which can be arbitrary in principle.

For small-amplitude waves, so-called weakly nonlinear approximations have been successful to derive equations more amenable to mathematical and numerical scrutiny for falling films [36]. Equations with a similar structure have actually played a very important role in the theoretical description of surface nanostructuring by IBS [10,25], hence it is instructive to see the form they take in our present case. Thus, for Eq. (1), we perform such a weakly nonlinear expansion of the irradiated thickness around the uniform-thickness solution h_0 (see Appendix A for details). We obtain the following equation for the perturbation, $\tilde{h}(x, y, t)$, around h_0 :

$$\begin{aligned} \tilde{h}_t = & -\tilde{a}_1\tilde{h}_x - \tilde{a}_2\tilde{h}\tilde{h}_x - a_2\tilde{h}^2\tilde{h}_x + h_0^2\nabla \cdot (\mathbf{B} \cdot \nabla\tilde{h}) + ch_0^3\nabla^2\tilde{h} \\ & + \nabla \cdot (\tilde{\mathbf{B}} \cdot \nabla\tilde{h}) - \gamma h_0^3\nabla^4\tilde{h} - 3\gamma h_0^2\nabla \cdot (\tilde{h}\nabla\nabla^2\tilde{h}), \end{aligned} \quad (3)$$

where $\tilde{a}_1 = a_1h_0 + a_2h_0^2$, $\tilde{a}_2 = a_1 + 2a_2h_0$, and $\tilde{\mathbf{B}} = 2h_0\mathbf{B} + 3ch_0^2\mathbb{I}$. This equation coincides with the perturbed anisotropic Kuramoto-Sivashinsky (KS) equation derived in Ref. [53] for a macroscopic film flowing down an inclined plane in the strong-surface-tension limit, save for linear third-order-derivative terms, absent from Eq. (3). In our case, nonlinearities include Burgers' (with coefficient \tilde{a}_2), the (anisotropic) derivative of a generalized Burgers term (with coefficient matrix $\tilde{\mathbf{B}}$), and a nonlinear contribution to surface-confined viscous flow (last term) [54]. At any rate, Eq. (3) already suggests that long-time properties of IBS nanopatterns, such as amplitude saturation, ripple shape, in-plane motion, and spatial structure, emerge as a balance among the nonlinearities induced by the streamwise and cross-stream components of the external driving, and by the stabilizing surface tension.

Formally, both partial differential equations, Eqs. (1) and (3), depend on five different physical parameters, namely, θ , G_s , G_b , μ , and σ . However, as shown in Appendix C, a suitable choice of coordinates allows us to rewrite a rescaled form of, e.g., Eq. (1) which depends on two dimensionless quantities only. These two parameter combinations can be chosen as the incidence angle θ and

$$\hat{g} \equiv \frac{2\sigma G_b}{9G_s^2}. \quad (4)$$

The dimensionless ratio (4) is analogous to the so-called Bond number in fluid mechanics [4,36], which quantifies the relevance of bulk (e.g., gravity) to surface forces. At any rate, once the relevant scale along the vertical direction has been fixed, e.g., via initial conditions or otherwise, the parameter

space for the continuum model, Eq. (1) or (3), is merely two-dimensional, being fully parameterized by θ , and the ensuing \hat{g} .

III. LINEAR REGIME: ANALYTICAL PREDICTIONS

As noted above, the full free-boundary system for the fluid velocity has been previously studied by means of linear stability analysis, for related IBS models [24,44–46,55]. In this section, we perform this type of analysis directly on the thickness equation, Eq. (1), to find that it is also quite informative in this case, as it retrieves the main qualitative properties of the onset of ripple formation as assessed in experiments [25]. Indeed, small periodic perturbations of the uniform solution, $h = h_0 + h_1 e^{i(q_x x + q_y y) + \omega t}$, evolve with linear dispersion relation

$$\begin{aligned} \omega(\mathbf{q}) = & -i(a_1h_0 + a_2h_0^2)q_x \\ & - h_0^2(b_1q_x^2 + b_2q_y^2 + ch_0q^2) - \gamma h_0^3q^4, \end{aligned} \quad (5)$$

where $\mathbf{q} = (q_x, q_y)$ is the 2D wave vector, $q = |\mathbf{q}|$, and $b_i = \mathbf{B}_{ii}$ ($i = 1, 2$). Perturbations grow in amplitude for \mathbf{q} such that $\text{Re } \omega(\mathbf{q}) > 0$. For positive values of σ and μ , the existence and range of unstable perturbations depend on the parameters reflecting the physical conditions for irradiation, G_b , G_s , and θ , the first two of which characterize the space distribution of residual stress and are expected to depend, primarily, on ion/target species combination and ion energy E [24]. Note that the precise polynomial form of $\omega(\mathbf{q})$ predicted by Eq. (5) has been validated recently by *in situ* x-ray analysis [32,56].

As also experimentally observed [25,31], for fixed E and ion/target combination, a morphological transition takes place at a critical incidence angle θ_c such that the flat solution is stable for $\theta < \theta_c$ and unstable for $\theta > \theta_c$. In this sense, the role of the ion incidence angle θ is analogous to that of the incline tilt for the macroscopic problem [4,36]. However, notably, the physical mechanism driving pattern formation is not inertia in the IBS case but, rather, the induced stress distribution. Indeed, assuming for definiteness a compressive value of the external stress at the free surface ($G_s > 0$), as obtained by MD for, e.g., Ar^+ irradiation of Si [24,41], b_1 becomes negative for $\theta > \theta_c$ and a band of unstable modes appears making positive the real part of the linear dispersion relation. Since $b_1 < b_2$ for all incidence angles, perturbations will grow along the x axis only if $b_1h_0^2 + ch_0^3$ is negative. Using the values for b_1 and c from Eq. (2), this requires that $\cos(2\theta) < -4g \cos(\theta)/9$, where

$$g \equiv \frac{G_b h_0}{G_s} \quad (6)$$

is a dimensionless quantity estimating the ratio between the stress jump across the fluidized layer and the stress value at the free interface. Such a simple expression of the space inhomogeneity of the ion-induced stress distribution has been seen in MD simulations [24] to play a central role for the pattern-forming behavior. If the uniform solution is $h_0 = 2\sigma/(9G_s)$, then $g = \hat{g}$ and, as anticipated in the previous section, the dynamics of Eq. (1) depends only on two parameters, the incidence angle θ and the dimensionless ratio g .

The critical angle for pattern formation, θ_c , at which $\cos(2\theta_c) = -4g \cos(\theta_c)/9$, can be obtained from the equivalent equation $2 \cos^2(\theta_c) + 4g \cos(\theta_c)/9 - 1 = 0$, which has the solution

$$\theta_c(g) = \arccos \left(-\frac{g}{9} + \sqrt{\left(\frac{g}{9}\right)^2 + \frac{1}{2}} \right). \quad (7)$$

This function, graphed in Fig. 1(b), tends to 90° for very large values of g and equals 0 for $g = -2.25$. Hence, a ripple structure emerges for $\theta > \theta_c$, periodic along the x direction, and with ripple crests along the y direction. As the value of θ_c depends on g , which in turn is expected to depend on irradiation conditions (like ion energy and ion/target combination) via $G_{s,b}$, Eq. (7) implies that θ_c is *not* a universal value across materials and energies. This lack of universality coincides with what is experimentally known [24,25] and emerges here for the first time as a prediction from a *nonlinear* thickness evolution equation.

Additionally, note that a zero-gradient, homogeneous stress distribution, namely, $G_b = g = 0$ implies $\theta_c = 45^\circ$, according to Eq. (1). Such a value for the critical angle was originally predicted in Ref. [57] via kinetic arguments on ion-induced material redistribution at the free surface. Finally, $\theta_c(g) = 0^\circ$ for $g = -2.25$ and is not defined for all (sufficiently negative) $g < -2.25$, which corresponds to a Bradley-Harper (BH)-like scenario in which ripples form for any incidence angle. Such a behavior was seminally predicted in Ref. [58] for sputtering-dominated IBS in competition with thermal surface diffusion. The 1D model proposed in Ref. [24] also accounts for a similar (albeit quantitatively different) BH-like scenario, the difference with our present result being possibly due to the different boundary condition employed. In what follows, we restrict ourselves to the non BH-like scenario, to date seemingly prevalent in experiments for clean monoatomic targets, [25] in which $\theta_c > 0^\circ$; hence, we consider $g > -2.25$.

Once a ripple pattern forms, it is predicted to have a wavelength $\lambda = 2\pi/q_*$, where \mathbf{q}_* is the wave vector which makes $\text{Re } \omega(\mathbf{q})$ a *positive* maximum. Thus, setting $\theta > \theta_c$ and optimizing Eq. (5), we obtain

$$\lambda = 2\pi/q_* = 2\pi \sqrt{\frac{-2\gamma h_0^3}{b_1 h_0^2 + c h_0^3}} \quad (8)$$

$$= 2\pi \sqrt{\frac{-4\sigma h_0}{9G_s \cos(2\theta) + 4G_b h_0 \cos(\theta)}}. \quad (9)$$

Actually, very close to pattern onset $\theta \gtrsim \theta_c$, its dependence on the incidence angle makes $\lambda(\theta)$ diverge, making this ripple formation a type-II transition in the pattern-formation terminology [2]. Type-II transitions are bifurcations in which the $q_* \neq 0$ stable solution branches out continuously from $q = 0$, hence being characterized by a length scale which diverges right at pattern onset (bifurcation point), akin to equilibrium continuous phase transitions [2]. Indeed, by Taylor-expanding the denominator of Eq. (8), we obtain

$$\lim_{\theta \rightarrow \theta_c^+} \lambda \approx 2\pi \sqrt{\frac{2\sigma h_0}{(9G_s \sin(2\theta_c) + 2G_b h_0 \sin \theta_c)(\theta - \theta_c)}} \sim |\theta - \theta_c|^{-1/2}. \quad (10)$$

Although to date there are not many experimental reports available on the value of the (critical) exponent n characterizing the observed $\lambda \sim |\theta - \theta_c|^{-n}$ divergence, those which exist [24,45,56] are consistent with the $n = 1/2$ value which is predicted by Eq. (10) to be universal, irrespective of, e.g., the precise value of the critical angle. From this point of view and continuing with the analogy with an equilibrium continuous phase transition, θ_c is akin to the critical temperature T_c , while n is analogous to the critical exponent characterizing the divergence of the system correlation length. As is well known, the value of T_c is not expected to be universal, as opposed to critical exponents [59].

Another pattern feature that can be analytically extracted within linear approximation [44,46,55] is the velocity for transverse ripple motion, namely, the velocity at which a local minimum of the linear ripple structure travels across the substrate, corresponding to the phase velocity of a wave mode [60]. Note that the imaginary part of Eq. (5) only depends on q_x , so that linear ripple motion takes place only in the x direction. In order to compute its velocity, we simply have to take the ratio between the imaginary part of the linear dispersion relation and the wave vector, both being evaluated at $\mathbf{q} = \mathbf{q}_*$, namely,

$$V = -\frac{\text{Im } \omega(\mathbf{q})}{q_x} \Big|_{\mathbf{q}=\mathbf{q}_*} = \frac{3G_s h_0 \sin(2\theta) + 4G_b h_0^2 \sin(\theta)}{2\mu}, \quad (11)$$

Perhaps even more intuitively, this result can also be obtained by considering the kinematic condition, Eq. (A8)—which states that the motion of the free interface is merely due to the fluid velocity field there—to lowest order within the perturbative expansion detailed in Appendix A. Thus under such an approximation Eq. (A8) becomes

$$h_t \simeq -u_0 h_x + w_1 = -V h_x, \quad (12)$$

where V is as in Eq. (11), u_0 and w_1 are the lowest-order non-trivial perturbative contributions of the u and w components of the velocity field [given by Eqs. (A18) and (A22)], and the last equality follows from the latter formulas after evaluation at $z = h$. Indeed, Eq. (12) describes a traveling wave moving along the x axis with constant speed V .

Provided ripples form, the condition $V = 0$ corresponds to $3 \cos(\theta) + 2g = 0$; equivalently, this condition introduces a g -dependent value of the incidence angle,

$$\theta_v(g) = \arccos \left(-\frac{2g}{3} \right), \quad (13)$$

which nontrivially separates experimental conditions characterized by a positive or a negative (linear) velocity for ripple transport when $g \in (-1.5, 0)$. This curve is shown as a dashed line in Fig. 1(b); to the left of the curve, the ripples move upstream with respect to the ion incidence, while ripples move downstream otherwise. For $g < -1.5$ (respectively, $g > 0$), the ripples always travel with a negative (respectively, positive) velocity, to linear approximation. Interestingly, for any fixed $g \in (-1.5, 0)$, the ripple velocity changes sign from positive (downstream) to negative (upstream) with increasing ion incidence angle θ .

Experimentally, in-plane ripple transport has been reported under conditions (ion energy and ion/target combination) like

the ones we are addressing here, e.g., in Refs. [61–64]. In particular, a dependence of the sign of the ripple transport velocity with incidence angle has been reported in experiments of 10-keV Xe⁺ ion irradiation of Si targets [63]. It is worth noting that both critical angles, θ_c and θ_v , depend on g and thus are expected to provide nonuniversal features for different energies, ions, and target materials.

IV. FULL DYNAMICS OF THE IRRADIATED LAYER

A. Numerical study

The results of the previous section have been derived within a linear approximation. Beyond elucidating the features of the pattern transition that takes place according to Eq. (1), they are confined to an early time regime within which the equation behaves similarly to its linearization around the homogeneous solution. For related previous models of IBS-induced viscous flow [24,44–46] the long-time (nonlinear) surface dynamics past such an early time behavior has thus far remained unexplored. In our present case, Eq. (1) now provides a means to additionally explore interface behavior deep into the nonlinear regime, while still reproducing analytically the main qualitative properties of the process within linear regime of evolution, described in Sec. III. Unfortunately, the strong nonlinearities occurring in Eq. (1) hamper further analytical progress. Hence, to assess the full dynamics of the irradiated layer, we have integrated numerically the strongly nonlinear 2D form, Eq. (1). Also, since weakly nonlinear formulations have played an important role in the field [25], when indicated and for the sake of comparison, we will also perform simulations of Eq. (3), namely, the weakly nonlinear approximation of Eq. (1).

In order to employ physically representative values of the equation parameters, accurate information on stress distributions is unfortunately very scarce. Hence, we consider order-of-magnitude estimates of parameters which are based on results for 1 keV Ar⁺ irradiation of Si [24,32,42], specifically, $G_s = 0.4$ GPa, $\sigma = 10$ GPa nm, $\mu = 0.83$ GPa min, and $h_0 = 5$ nm. We will study several conditions on the stress gradient G_b within the irradiated layer, implying up to three different values of g . For each of them, we will study two values of the incidence angle above the corresponding $\theta_c(g)$, leading to the six parameter conditions (a) through (f) described in Table I and indicated graphically in Fig. 1(b). Specifically, we will consider one condition for $G_b = -0.1$ GPa nm⁻¹, in which the external stress becomes less compressive along the ion-beam direction. This induces $g = -1.25 \equiv g_1$ and $\theta_c(g_1) = 30.7^\circ$. Our second stress condition with $G_b = 0.05$ GPa nm⁻¹ reverses the sign of g so that the ion-induced stress becomes increasingly compressive along the ion-beam direction, with $g = 0.625 \equiv g_2$ and $\theta_c(g_2) = 50.1^\circ$. We finally consider a third value of the stress gradient, $G_b = -0.06$ GPa nm⁻¹, which induces a reduced negative $g = -0.75 \equiv g_3$ in such a way that the linear ripple velocity can change sign as a function of the incidence angle. For this parameter choice, $\theta_c(g_3) = 60^\circ$. We combine a fourth-order Runge-Kutta scheme for time with finite differences in space, using periodic boundary conditions and a lattice (time) step of 1 nm (10⁻⁵ min), guaranteeing that mass is conserved and that

results do not differ significantly for smaller space and time steps. The initial thickness is $h = h_0$, perturbed by zero-mean, Gaussian white noise with 0.1 nm standard deviation.

B. One-dimensional systems

Many of the main features of the present pattern-forming process can already be quite accurately retrieved when studying one-dimensional systems in which the y dependence is dropped altogether. Recall that, e.g., when ripples form, their periodicity is along the x direction as discussed in Sec. III. Thus, in this section, we first address this simpler setting through numerical simulations of the 1D counterparts of the strongly nonlinear equation Eq. (1) which, in conservative form, reads

$$h_t = -[a_1/2h^2 + a_2/3h^3 - b_1h^2h_x - ch^3h_x + \gamma h^3h_{xxx}]_x \quad (14)$$

and, when appropriate, of its weakly nonlinear approximation Eq. (3), namely,

$$\begin{aligned} \tilde{h}_t = & -[\tilde{a}_1\tilde{h} + (\tilde{a}_2/2)\tilde{h}^2 + (a_2/3)\tilde{h}^3 - (h_0^2b_1 + ch_0^3)\tilde{h}_x \\ & - \tilde{b}_1\gamma h_0^3\tilde{h}\tilde{h}_x\tilde{h}_{xxx} + 3\gamma h_0^2\tilde{h}\tilde{h}_{xxx}]_x, \end{aligned} \quad (15)$$

where $\tilde{b}_1 = \tilde{\mathbf{B}}_{11}$. Note that one advantage of the latter equation is that, while being nonlinear, it incorporates the basic properties of the linear stages of evolution in a fully explicit form, in contrast with Eq. (1). For instance, the linear terms in Eq. (15) readily retrieve the linear dispersion relation, Eq. (5) (setting $q_y = 0$), including both, the contribution (Re ω) which accounts for ripple formation and amplification/decay and the contribution (Im ω) which described the ripple transport velocity, Eq. (11). Actually, a similar consideration applies to the 2D weakly nonlinear equation, Eq. (3), in that case for arbitrary values of q_y .

We first consider the way in which the sign of the stress gradient across the irradiated layer influences the dynamics. Thus Fig. 2 shows fixed-time frames of the layer at relatively long times within the nonlinear regime, as described by the 1D strongly nonlinear equation, Eq. (14); the frames are taken from movies available in Ref. [65]. Specifically, movies 1D_movie_50deg_Gb=-0.1 and 1D_movie_60deg_Gb=-0.1 show the time evolution of a 120 nm portion of the system (the actual system size of these simulations was 300 nm) for $g = g_1 < 0$ with $\theta = 50^\circ$ and 60° , respectively [(a) and (b) conditions in Table I]. Similarly, movies 1D_movie_60deg_Gb=0.05 and 1D_movie_70deg_Gb=0.05 show the time evolution of the 1D irradiated layer for $g = g_2 > 0$ under $\theta = 60^\circ$ and 70° , respectively [conditions (c) and (d) cases in Table I]. The pressure and velocity fields in the irradiated layer were solved perturbatively as functions of the local thickness h , to which they are enslaved [36] and are shown in these movies and in Fig. 2 (see details in Appendix A). Figure 2 readily illustrates how, on average, the pressure decreases with depth across the irradiated layer for $g < 0$ while it increases, as intuitively expected, for $g > 0$. The pressure field is not $x \leftrightarrow -x$ symmetric, differing markedly on both sides of the ripples, while the velocity field also reflects the morphology of the free interface. These

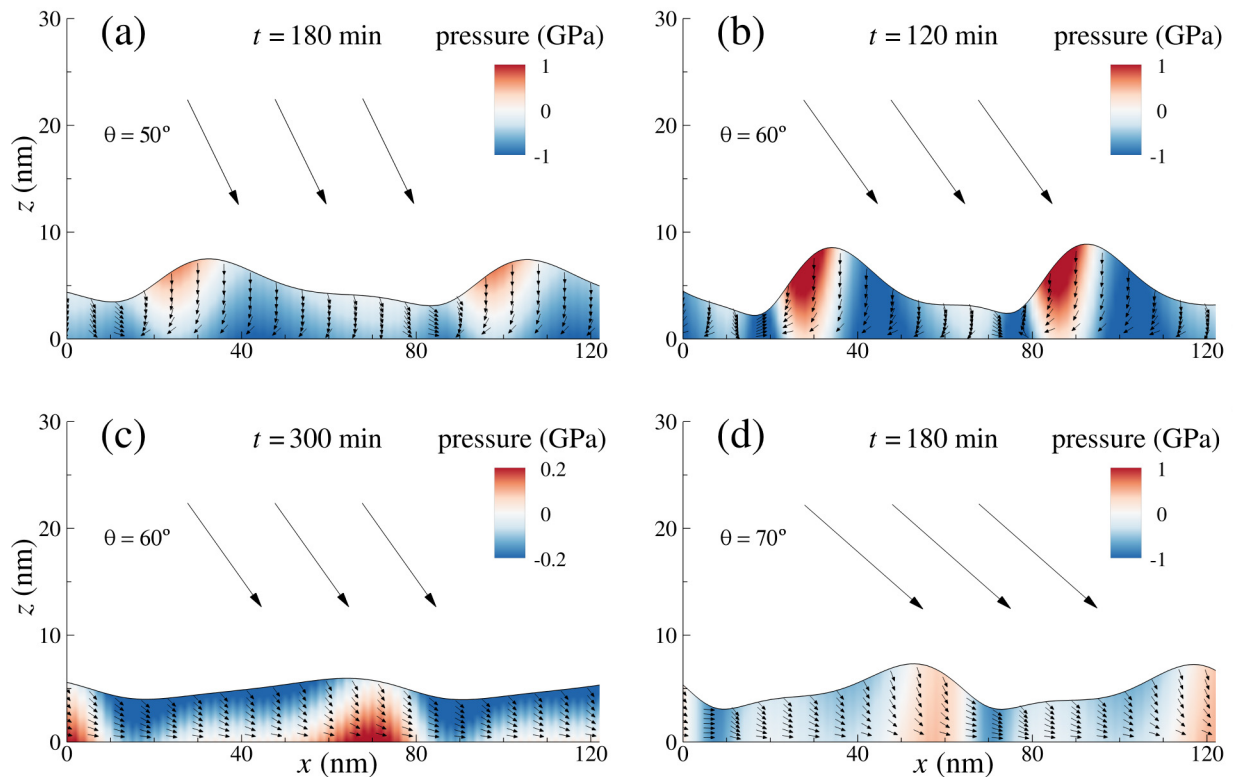


FIG. 2. Irradiated layer according to the 1D strongly nonlinear equation, Eq. (14), (no y dependence) for the parameter conditions (a)–(d) defined in Table I. The fluid pressure (velocity) is shown as a color (vector) field and the large arrows represent the ion beam incidence direction.

velocity fields resemble the displacement vectors obtained by MD simulation calculated at two different snapshots [31].

Indeed, for all parameter conditions (a) through (d), a morphological ripple-forming instability occurs which remains within linear regime for tens of minutes, as in experiments [25]. Detailed inspection of the pressure and velocity fields in the movies allows one to trace back the origin of the instability to the coupling between the differential exposure of initial height perturbations to the ion beam and fluid incompressibility: fluid excess (due to slowing down) at the free interface leads to interface corrugation due to incompressibility; for large enough θ , such a disturbance becomes amplified and eventually ripples form. The amplification of the most unstable mode of the thickness leads to a fast increase of the global surface roughness $W(t)$ (root-mean-square fluctuation of h around its mean value) with time within this linear instability regime, the ripples being sinusoidal undulations with a wavelength given by Eq. (8). For the sake of comparison, Fig. 3 shows the roughness as obtained for both, the strongly and the weakly nonlinear equations, Eqs. (14) and (15), for the same parameter conditions. Although some quantitative differences exist (e.g., dynamics seem to be faster for any given condition in g , according to the weakly nonlinear equation) the qualitative behaviors are quite similar.

At longer times, the ripples cease to be sinusoidal, nonlinearly evolving into asymmetric cross-sections, which eventually reach stationary amplitudes of a few nanometers. A steady state seems to be eventually reached in which the global surface roughness W becomes time-independent, see Fig. 3, as is known to happen in experiments [25]. This occurs

faster for the weakly nonlinear equation than for the strongly nonlinear form, for any value of g , with somewhat stronger fluctuations of W around the corresponding steady-state value in the former case too. The (nonlinear) ripple wavelength λ (peak-to-peak distance) reached at steady state becomes at least ten times larger than the ripple amplitude (note the different scales for the horizontal and vertical axes in Fig. 2), also akin to experiments and consistent with our thin-film approximation. For fixed g , namely, fixed energy and ion/target combination, λ decreases (while global roughness and ripple amplitude both increase) with increasing ion incidence angle θ , dynamics being faster both within the strongly and the weakly nonlinear descriptions (in particular, the corresponding steady state is reached earlier), again in accordance with experimental observations [25]. Finally, dynamics are also faster for $g = g_1$ than for $g = g_2$ for comparable values of the angle of incidence, cf. the movies provided in Ref. [65] and note the time values indicated in Fig. 2. This is due to the fact that θ_c is an increasing function of g , see Fig. 1(b), hence the values of θ employed for these simulations at higher g are closer to the corresponding critical angle, for which dynamics are slower as explained above, and consistent (as is the faster dynamics with increasing θ for a fixed value of g) with critical slowing down at a type-II pattern-forming transition [2].

In all our simulations, ripple motion is readily seen to take place along the substrate plane. Both within the linear and the nonlinear time regimes, this motion proceeds as described by Eq. (12), specifically in the direction implied by the sign of V in Eq. (11): upstream for $g = g_1$ and downstream for $g = g_2$, see Fig. 1(b). Remarkably, nonlinear effects do not

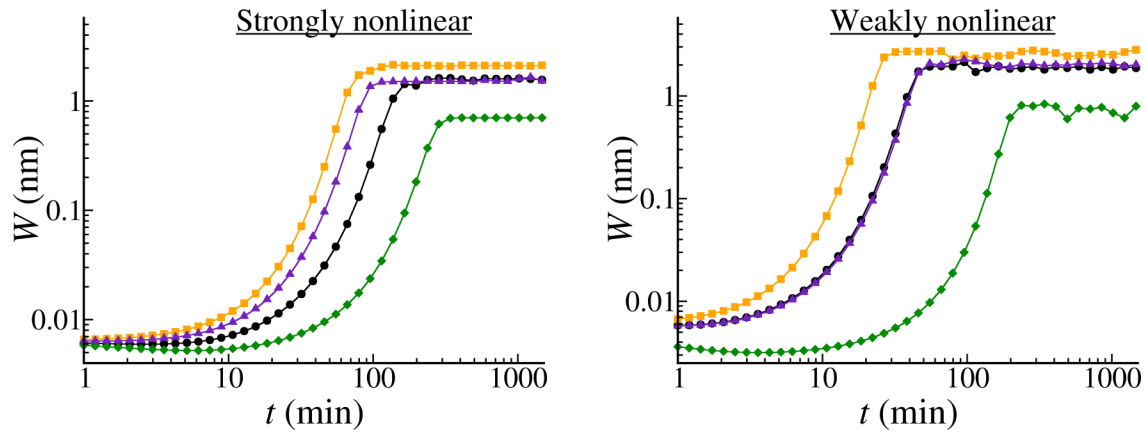


FIG. 3. Temporal evolution of the surface global roughness $W(t)$, according to the 1D strongly nonlinear equation, Eq. (14) (left) and to its 1D weakly nonlinear form, Eq. (15) (right). Black circles, orange squares, green diamonds, and violet triangles represent, respectively, the parameter conditions (a)–(d) specified in Table I.

seem to substantially change such a prediction on the direction of motion, which in principle has been derived from the linear analysis in Sec. III. This remains the case even for parameter conditions with $g = g_3$, for which the direction of ripple motion can change with the incidence angle θ . The full dynamics of the 1D irradiated layer for such a value of g is shown in movies 1D_movie_50deg_Gb=-0.06 and 1D_movie_70deg_Gb=-0.06 provided in Ref. [65] obtained from numerical simulations of Eq. (14) and corresponding to $g = g_3$ under $\theta = 50^\circ$ and 70° , respectively [conditions (e) and (f) in Table I]. Sample fixed-time frames of these movies are shown in Fig. 4 for relatively long times within the nonlinear regime. When comparing conditions (e) and (f) in Table I, all qualitative considerations regarding wavelength and roughness behavior still apply, analogous to the comparisons among cases (a) through (d) for fixed g . The most striking difference is that ripples now move downstream for condition (e) ($\theta = 50^\circ$), while they reverse direction and become transported upstream for a higher $\theta = 70^\circ$ under condition (f). Experimental reports on ripple motion are comparatively few (e.g., Refs. [62,66–68], reviewed, e.g., in Refs. [25,69]), there being even less where the direction of motion is correlated with the dominance of nonlinear effects and/or the stress

distribution in the irradiated layer. Hence, our present observation provides a prediction towards future model validation, especially under conditions featuring a small sputtering rate.

The $x \leftrightarrow -x$ asymmetry of the ripple structure can be also underscored as a further morphological property of the ripples in the nonlinear time regime, which is also well-documented in experiments [25]. Recall that Eqs. (1) and (14) generalize the equations put forward by Bertozzi *et al.* in Refs. [51,52] through the additional term proportional to \mathbf{B} , absent from the continuum model studied in these references. Still, this model has been characterized in detail with respect to the asymmetric nonlinear ripple shapes it can describe [51,52] depending on parameter conditions, so that it provides a relevant reference case for our present continuum model. The context for the comparison is that of shock formation, which is a natural one in the presence of a Burgers nonlinearity. Indeed, the inviscid Burgers equation is well known to lead to shock formation [70]. Since in our case $a_1 > 0$, this would imply a shock breaking towards positive x . Neglecting the \mathbf{B} term in Eq. (1), this is expected to still be the case as long as $g > 0$ [71], which agrees with the asymmetry found numerically for the ripples corresponding to conditions (c) and (d) in Table I, see Fig. 2. Considering $g < 0$ opens the possibility to the occurrence of

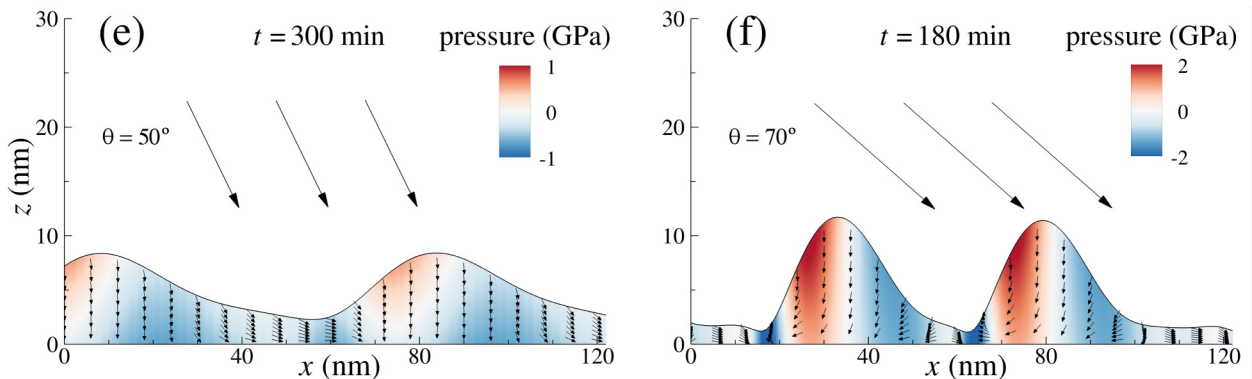


FIG. 4. Irradiated layer according to the 1D strongly nonlinear equation, Eq. (14) (no y dependence) for the parameter conditions (e) on the left and (f) on the right defined in Table I. The fluid pressure (velocity) is shown as a color (vector) field and the large arrows represent the ion beam incidence direction.

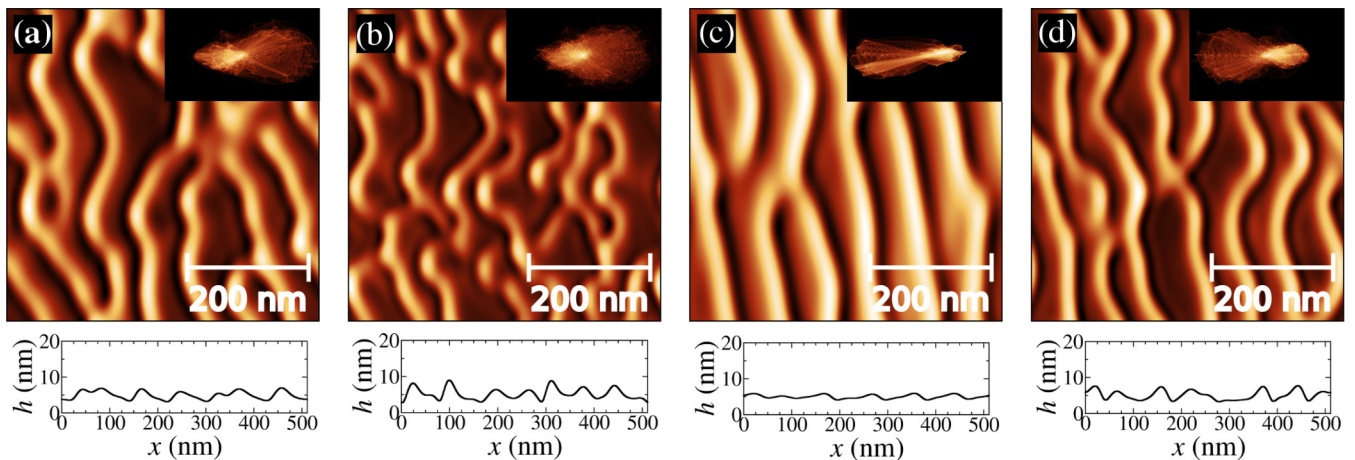


FIG. 5. Free interface (top view) according to the 2D strongly nonlinear equation, Eq. (1), at $t = 425$ min for the cases (a)–(d) defined in Table I. The insets display the corresponding slope distributions. The bottom images show horizontal transverse cuts along the projection of the ion beam direction (x axis) in the middle of the corresponding 2D topography.

less standard, so-called undercompressive shocks in which information travels away from the shock [51,52,71,72], in contrast with classical, so-called compressive, shocks [70]. In our simulations of Eq. (14) for $g < 0$ with $|G_b| \simeq 1$, we can note that the asymmetry of the ripple structure reverses with respect to the $g > 0$ case, see conditions (a) and (b) in Fig. 2, while roughly symmetric ripples are found for much smaller values of $|G_b|$, see Fig. 4 for conditions (e) and (f) in Table I. Undercompressive shocks have been previously reported in the description of IBS systems via kinetic (rather than hydrodynamic) continuum models [30,73–77]. The connection between such undercompressive shocks and sawtooth morphologies has been specifically addressed in Refs. [30,76], where nonlinear effects have been demonstrated to be able to reverse the direction of ripple motion under suitable conditions.

C. Two-dimensional systems

Beyond 1D systems, nonlinear continuum models such as Eqs. (1) and (3) are able to describe the dynamics of the irradiated layer taking into account the full 2D dependence on the (x, y) coordinates of the substrate plane. The qualitative features of the pressure and velocity fields are analogous to those seen in the previous section. Hence, here we choose to focus on the dynamics of the free surface of the irradiated layer. Thus, to appreciate the full 2D dependence of $h(x, y, t)$, the temporal evolution of the surface morphology for a 512×512 nm² system is shown in the movies available in Ref. [65], whose naming code follows the one employed for the 1D movies. Figure 5 provides four top-view fixed-time frames from these movies at relatively long times within the nonlinear regime, corresponding to the parameter values (a) through (d) indicated in Table I. For the sake of comparison, Fig. 6 displays analogous results from numerical simulations of the 2D weakly nonlinear equation, Eq. (3).

As expected for many KS-related systems [36,78] and as seen in experiments [25], the ripples become increasingly disordered with continuing irradiation, this process being faster for larger θ at fixed g . Such a behavior can be quantitatively

assessed, e.g., via the slope distributions shown in the insets of Fig. 5, which also speak of the asymmetry of the nonlinear ripple cross-sections, already noted in Fig. 2. Specifically, these slope distributions are 2D plots in which the independent variables are the space derivatives of the layer thickness, $m_x = h_x$ and $m_y = h_y$, along the two coordinate directions on the 2D topographical image; the dependent variable is the fraction of points (using a logarithmic scale) of this topography at which the slopes happen to equal the pair of values (m_x, m_y) ; the data processing was performed using GWYDDION 2.44 software [79]. The fraction of points with slopes $(m_x = 0, m_y = 0)$ is depicted in the center of each inset in Fig. 5. Thus the streamwise asymmetric shape of the ripples in the nonlinear time regime, already seen in the 1D simulations, can be quantitatively assessed for the full 2D topographies as well. Since the positive slopes along the streamwise direction (x axis) reach larger absolute values in Figs. 5(a) and 5(b), the distributions of the positive slopes along this direction (graphed in the right sides of the corresponding insets) are wider than the distributions for the negative slopes (graphed in the left sides of the insets). The opposite behavior of larger absolute values for negative slopes is found for the morphologies of Figs. 5(c) and 5(d). These differences increase with time from the more symmetric topographies during the linear regime to the more asymmetric morphologies in the saturated nonlinear stages. Regarding the slopes along the cross-stream direction (y axis), the slope distributions are wider for more disordered morphologies such as Fig. 5(b) than for better arranged ripples as in Fig. 5(c).

Completely analogous results on the 2D morphological dynamics are provided by numerical simulations of the weakly nonlinear equation Eq. (3), see Fig. 6. The ripple asymmetry and the level of disorder along the cross-stream direction are very similar to those predicted by Eq. (1) when the same parameter values are employed. Possibly the main difference between both continuum models is the somewhat faster dynamics for the weakly nonlinear equation, which was already noted for the 1D case, see Fig. 3. This feature can be likewise noticed in Fig. 7, where the temporal evolution of the height global roughness $W(t)$ for Eqs. (1) and (3) are graphed for

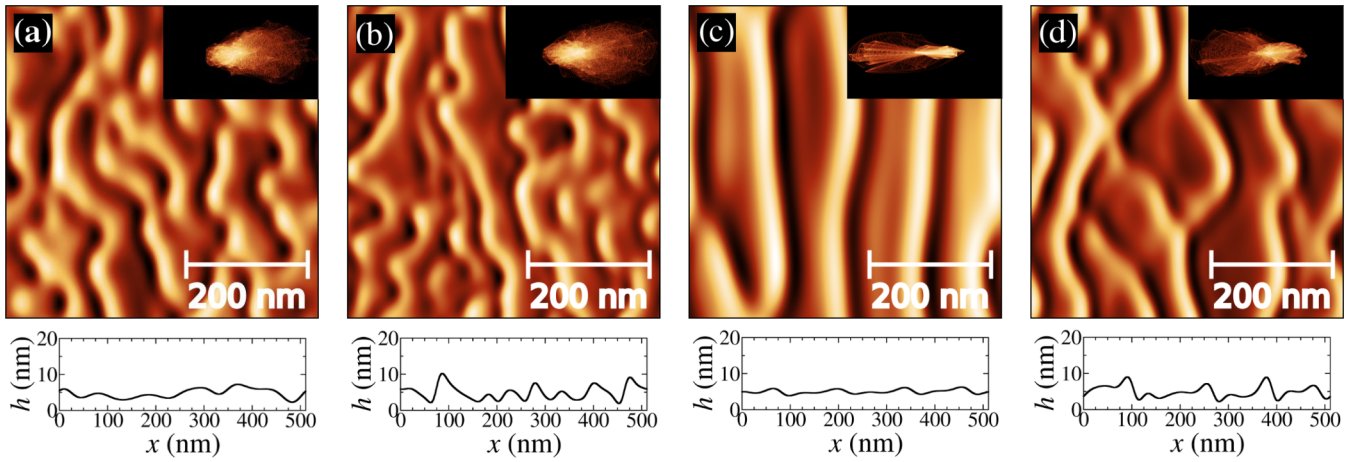


FIG. 6. Free interface (top view) according to the 2D weakly nonlinear equation, Eq. (3), at $t = 425$ min for the cases (a)–(d) as indicated in Table I. The insets display the corresponding slope distributions. The bottom images show the corresponding horizontal transverse cuts along the projection of the ion beam direction (x axis) in the middle of the topography.

the same parameter values. This figure again indicates faster dynamics for larger θ values at a fixed value of g . The exact exponential function which is graphed as a reference [recall that $W(t)$ grows exponentially with time within the linear regime] suggests fast saturation of the roughness to a steady-state value once nonlinear effects set in, both within the strongly and the weakly nonlinear descriptions. However, fluctuations around the steady state value are substantially stronger in 2D than in 1D, specially in the case of the strongly nonlinear equation, possibly due to the progressive disordering which takes place along the y direction, compare Figs. 3 and 7 from this point of view.

This interpretation is substantiated more quantitatively by Fig. 8, which shows the power spectral density (PSD) along the x and y directions for different values of time, as obtained e.g., from numerical simulations of Eq. (1) for parameter condition (a) in Table I (analogous conclusions can be drawn for other parameter conditions, not shown). Here, we define the 2D height PSD as $\text{PSD}(\mathbf{q}, t) = |\hat{h}(\mathbf{q}, t)|^2$,

where $\hat{h}(\mathbf{q}, t)$ is the space Fourier transform of $h(x, y, t) - \bar{h}(t)$, bar denotes space average. The PSDs shown in Fig. 8 are for 1D cuts of the 2D morphologies; equivalently, they can be considered as the wave-vector integrals of $\text{PSD}(\mathbf{q}, t)$ along the q_y or q_x axes, $\text{PSD}_x(q_x, t) = \int \text{PSD}(\mathbf{q}, t) dq_y$ and $\text{PSD}_y(q_y, t) = \int \text{PSD}(\mathbf{q}, t) dq_x$, respectively. The position, q_* , of the main local maximum of PSD_x by the end of the linear regime ($t = 92$ min) corresponds to the (inverse of the) ripple wavelength, which is seen to remain basically unchanged for longer irradiation times. The existence of the secondary maxima in PSD_x moreover attests to a rather well-defined ripple form along the x direction. However, the relative value $\text{PSD}_x(q_*, t)/\text{PSD}_x(q_x, t)$ decreases with increasing time for $q_x \neq q_*$, as a reflection of the increasing disorder in the ripple arrangement along the x direction seen in Fig. 6. Along the transverse y direction no such characteristic relative maximum of PSD_y exists; rather, a value of q_y does separate q -independent from q -dependent behavior in PSD_y . While such a value seems to change from the linear (compare $t = 92$ with

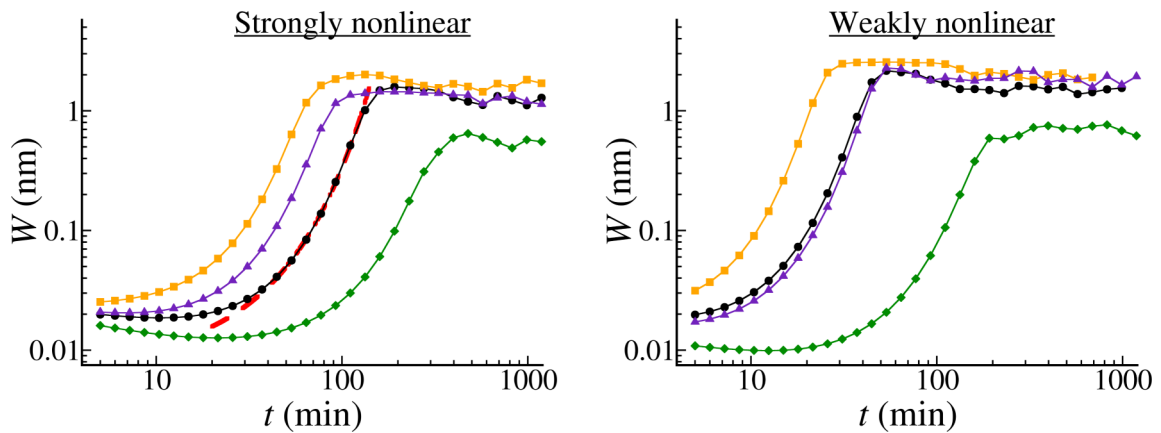


FIG. 7. Temporal evolution of the surface global roughness, $W(t)$, according to the 2D strongly nonlinear equation, Eq. (1), (left figure) and to the 2D weakly nonlinear equation Eq. (3) (right figure). Black circles, orange squares, green diamonds, and violet triangles represent, respectively, the cases (a)–(d) in Table I. As a reference, the dashed red line in the left figure graphs the exponential growth given by the function $0.007 e^{0.038t}$.

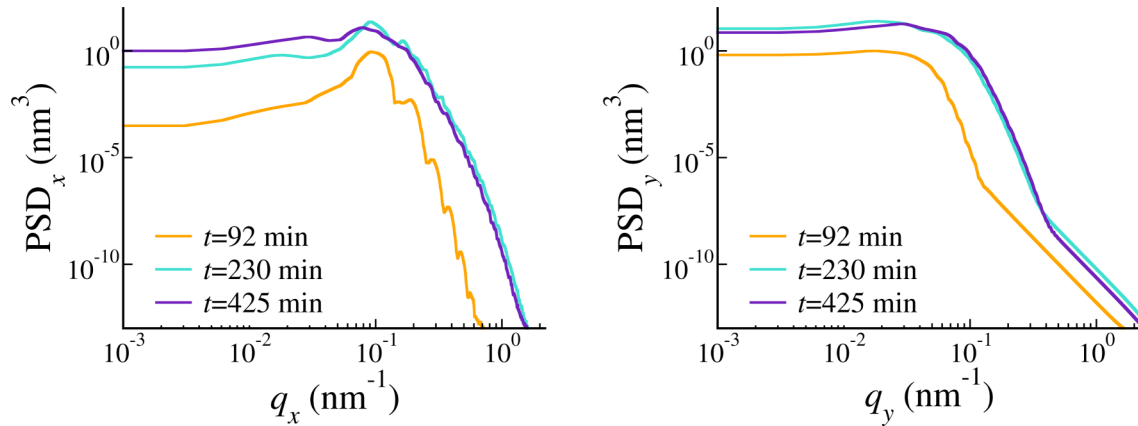


FIG. 8. Height power spectral density (PSD) of the free interface according to the 2D strongly nonlinear equation Eq. (1) at different times along the streamwise direction, x axis, (left figure) and cross-stream direction, y axis, (right figure), for parameter condition (a) in Table I.

$t = 230$ min) to the nonlinear regime, it seems to saturate within the latter (compare $t = 230$ with $t = 425$ min). At any rate, the value of PSD_y increases substantially for all q_y , from the linear to the saturation regime, at which PSD_y values are comparable to, or even larger than, PSD_x values, speaking of the substantial disorder which also occurs in the morphology along the y direction. Globally, the nonlinear ripple dynamics described by our continuum model corresponds to a progressive disordering of the pattern in the two substrate directions, which takes place at a rate that depends on the value of the incidence angle, much as seen in impurity-free experiments [25]. From the point of view of this description and within the physical assumptions that we have made, patterns with improved spatial ordering are to be sought for under more elaborate irradiation settings, such as, e.g., cases including impurity co-deposition, the application of multiple beams sequentially or simultaneously, and/or employing pretreated targets, see an overview in Ref. [25].

V. FURTHER DISCUSSION AND CONCLUSIONS

Summarizing our results thus far, we have derived a nonlinear continuum model of surface dynamics for solid targets which either are or become amorphous under ion-beam bombardment at low-to-medium ion energies. Our model builds upon the assumption that this surface nanopatterning method is largely driven by the relaxation of the residual stress induced by irradiation, via Newtonian viscous flow of the topmost surface layer of the target, whose thickness is of the order of the ion range. In order to unambiguously assess the implications of this assumption for the full evolution of the system, we have neglected the occurrence of erosion (sputtering), a working condition which has been demonstrated experimentally very recently in the context of nanoripple formation [31]. Still, according to these experimental results, a negligible sputtering yield does not preclude the ensuing surface morphological behavior from sharing many qualitative features with what is seen under non-negligible sputtering conditions [25]. Moreover, even in the latter case, the fact that the observed critical angles for pattern formation are nonzero suggests that onset for ripple formation is due to physical mechanisms other than sputtering.

Previous theoretical continuum models addressing the same class of experiments as we presently do, have been restricted to a number of partial issues and to linear stability analysis. In contrast, a distinctive feature of our present approach is the attempt to describe the full time evolution of the system—from the early times at which the ripple instability sets in to the long times at which nonlinear properties unfold, such as, e.g., asymmetric ripple shapes—within a single framework, provided by a nonlinear evolution equation for the thickness of the irradiated layer. An important requirement is that such a model reproduces the main qualitative features of the onset of ripple formation, which have been established experimentally [25] and which were already amenable to prior theoretical works dealing with the linear regime of evolution. Such features, which are indeed reproduced by Eq. (1), include the following: (1) a type-II morphological transition between a flat and an anisotropic rippled surface that occurs at a nonzero critical angle $\theta_c \neq 0$; (2) a linear dispersion relation consistent with the KS polynomial structure $\omega \sim q^2 - q^4$; (3) nonuniversal values (i.e., values which can change with ion energy and/or ion-target species combination) of θ_c and of the linear ripple wavelength λ ; (4) a universal (i.e., independent of energy and atomic species) value of the critical exponent which characterizes the divergence of $\lambda(\theta)$ for $\theta \gtrsim \theta_c$; (5) faster dynamics for increasing $\theta > \theta_c$; and (6) a nontrivial dependence of the velocity of ripple transport with irradiation conditions.

To date, the ingredients and parameters entering our theoretical model, such as the space variation of the residual stress distribution, and the ion-induced viscosity and surface tension, are only known with large experimental and theoretical uncertainties, as are their dependencies with irradiation conditions, like ion energy and atomic species. Hence, the agreement between our present model and experiments remains qualitative. Nevertheless, our results provide us with parsimonious explanations for certain experimental behaviors. Take, for instance, the lack of universality in the value of θ_c , which in our model originates in its dependence with the dimensionless parameter g , recall Eq. (7). This fact provides a clue to understand the disparity of critical angles reported in the literature. In particular, it seems that low energy ($E < 1$ keV) Ar^+ irradiation of Si targets leads to a robust value

around 45° [24,42,45,80]. According to Fig. 1(b), this fact suggests that $g \simeq 0$, physically implying that the bulk stress is quite homogeneous in these experiments. For higher energies [81], θ_c seems to be around 40° , which would predict a negative value of g . This implies that stress changes with depth, perhaps a consequence of the existence of Ar bubbles of different diameters within the amorphous layer. On the other hand, by increasing the ion mass (Ar⁺ to Kr⁺ to Xe⁺), θ_c also increases [24,82,83], suggesting that bulk effects become more relevant as the ion mass increases. In general, this type of trends in experimental parameters are suggestive of model properties (e.g., signs and absolute values of g) to be confirmed by, e.g., future MD simulations. In this connection, recall the BH-like scenario we described above for $g < -2.25$, to be realized perhaps under different irradiation conditions, like, e.g., concurrent impurity deposition [24,25].

On the other hand, the available order-of-magnitude estimates for our model parameters, once fed into our numerical simulations, do yield patterns with typical time and length scales that compare quite favorably with experimental results, as shown in Figs. 2 through 8. These figures even compare well (qualitatively and semiquantitatively, in the present sense) with specific experimental topographies at long fluences, like, e.g., ripples produced on glass [62] or on a Cd₂Nb₂O₇ pyrochlore single crystal [67] under oblique angle bombardment by 30 keV Ga⁺ ions. However, the predictive power of our model is still far from being able to compute the precise values of g for such experiments and then producing images which accurately match the experimental topographies.

Another virtue of our present (fluid dynamical) approach is to provide us with detailed information on the space distribution and time evolution of additional relevant physical quantities within the irradiated layer, namely, the pressure and velocity fields. While these are amenable to comparison with estimates/measurements from more atomistic modeling like MD simulations, which can eventually enable model refinements, they are also instrumental to elucidate the physical nature of the linear morphological instability, as the interplay between differential driving and fluid incompressibility. Actually, they also allow us to make explicit the complex near-surface dynamics which eventually unfolds into nonlinear surface properties. Among those with ample experimental basis [10,25] which are accounted for by the long-time evolution of Eq. (1), we can quote (1) amplitude stabilization at realistic times; (2) (lack of) ripple wavelength coarsening; (3) small [$\sim O(10^{-1})$] amplitude-to-wavelength ratios; (4) asymmetric ripple shapes; (5) nontrivial ripple motion (e.g., direction reversal), contingent upon experimental conditions; (6) ripple disordering along the two substrate directions; and (7) enhanced ripple disorder for increasing $\theta > \theta_c$.

Some of these properties actually call for more detailed experimental information which does not seem to be currently available, and which would be interesting as further validation of our present model. For instance, the occurrence of the critical angle θ_v for reversal of ripple motion, and the correlation between the asymmetry of ripple cross sections and direction of motion in the nonlinear stages of evolution.

Still, a number of nonlinear properties which have been also reported experimentally [10,25] do not seem to be

captured by Eq. (1), including, e.g., (1) ripple coarsening, (2) kinetic roughening, and (3) secondary pattern features beyond main symmetry and wavelength.

There are many potential sources for these discrepancies, which range from methodological to physical. (i) Even if our continuum models are adapted to probing large scale properties, our simulations of Eqs. (1) or (3) are still affected by computational limitations to accessible physical times and system sizes. (ii) Even restricted to a fluid flow description, a number of assumptions can be relaxed and improved upon. Thus one can consider improved (more realistic) boundary conditions at the i/u interface, the space distribution of stress can be more complex than that described by a linear polynomial, and the constitutive relation between ion-induced strain and stress can be generalized beyond the Newtonian fluid approximation. (iii) A number of important physical mechanisms need to be eventually incorporated, most notably erosion (sputtering) [58,84] and ion implantation [85], whose relative contributions to the morphological stability of the surface can compete in nontrivial ways. In principle, we do not expect substantial qualitative changes in the system behavior from sources of types (i) and (ii); technically, the form of the terms contributing to, e.g., the weakly nonlinear form of the evolution equation is quite robust to detailed changes in the form of, e.g., the space distribution of stress, which are relatively minor to change the system behavior close to pattern onset. Still, explicit confirmation seems in order, especially working under far-from-equilibrium conditions as in our present context. Sources of type (iii) for different behavior do also require explicit formulation and study, and also remain as a topic for future work, hopefully leading eventually to accurate predictions on system properties like θ_c and θ_v , which correctly reflect the specific irradiation conditions.

Last but not least, note that, while the morphologies described by Eq. (1) do reproduce quite closely IBS experiments on, e.g., glass [62,66] or Cd₂Nb₂O₇ pyrochlore [67], they also strongly resemble images of macroscopic fluid films flowing down an incline [36,86]. Although the length scales of the two problems differ by a 10^5 factor, timescales are notably similar. This speaks of the huge timescale separation between microscopic dynamics and collective behavior in IBS, at the core of challenges to its theoretical description. In general, the links between Eqs. (1) or (3) and nonlinear descriptions of classic problems like fluid flow down an inclined plane attest to the great universality that exists in the self-organization of matter. Moreover, the large body of knowledge on nonlinear behavior that has been developed for the macroscopic system [36–39,53] may partially carry over to a nanoscopic setting, thus serving to elucidate novel phenomena in nanofluidics, a fascinating frontier for fluid dynamics. We have discussed one such connection in Sec. IV B, related to the dynamics of (compressive and undercompressive) shocks, but additional ones may be foreseen, contributing to a potentially fruitful cross-fertilization of fields.

ACKNOWLEDGMENTS

We thankfully acknowledge discussions with R. M. Bradley, R. Gago, A. Moreno-Barrado, A. Redondo-Cubero, and L. Vázquez. This work is partially supported by

Ministerio de Economía y Competitividad, Ministerio de Ciencia, Innovación y Universidades, Agencia Estatal de Investigación, and Fondo Europeo de Desarrollo Regional (Spain and European Union) through Grants No. FIS2015-66020-C2-1-P, No. FIS2015-73337-JIN, No. FIS2016-78883-C2-2-P, No. BIO2016-79618-R, and No. PGC2018-094763-B-I00.

APPENDIX A: ANALYTICAL DERIVATION OF THE EVOLUTION EQUATION FOR THE FREE INTERFACE

The solid flow description of IBS [24,44–46] is based on the fact that, as a consequence of the impact of the ions and the subsequent release of energy within the target, residual stress is confined to a thin superficial amorphous layer. The incoming ions induce fluidity of such an amorphous film, characterized by a slow time relaxation. This highly viscous flow will be assumed to be incompressible, and therefore its velocity \mathbf{v} verifies

$$\nabla \cdot \mathbf{v} = 0. \quad (\text{A1})$$

Since the temporal derivative is not considered in the Cauchy equation for this noninertial viscous flow, the equation describing momentum transport reduces to [4,36]

$$\nabla \cdot \mathbf{T} = \mathbf{0}, \quad (\text{A2})$$

where the stress tensor $\mathbf{T} = \mathbf{T}^F + \mathbf{T}^{\text{ext}}$ is the sum of the fluidic contribution $\mathbf{T}^F = -p\mathbb{1} + \mu(\nabla\mathbf{v} + \nabla\mathbf{v}^T)$ (where μ , p , and $\nabla\mathbf{v}$ are the viscosity, the hydrostatic pressure, and the Jacobian matrix of \mathbf{v} , respectively) and an external contribution \mathbf{T}^{ext} due to the strain induced by the irradiation. Equations (A1) and (A2) provide a connection between the fluid pressure $p(\mathbf{r}, t)$ and the velocity components $\mathbf{v}(\mathbf{r}, t) = (u(\mathbf{r}, t), v(\mathbf{r}, t), w(\mathbf{r}, t))$ at any point \mathbf{r} and time t . The laboratory coordinate system $\mathbf{r} = (x, y, z)$ is chosen so that the z axis is perpendicular to the initially planar target and the x axis is oriented along the projection of the incoming ions on the surface [see Fig. 1(a) in Sec. II].

Molecular dynamics (MD) simulations have shown that the generation of stress across the damaged amorphous layer may be characterized by a diagonal matrix with negligible trace [24], depending only on the distance to the free surface [24,41]. Hence, in a coordinate system (x', y', z') , with z' oriented in the opposite direction to the ion beam, we assume the irradiation-induced stress tensor to be

$$\mathbf{T}^{\text{ext}'} = \tau(z') \begin{pmatrix} 1 & 0 & 0 \\ 0 & 1 & 0 \\ 0 & 0 & -2 \end{pmatrix}, \quad (\text{A3})$$

where the stress amplitude τ describes the cumulative damage induced by the irradiation. We can write this tensor in the laboratory coordinate system considering that the incidence angle with respect to the z axis is θ and that the rotation matrix about the negative y axis in three-dimensional space reads

$$R = \begin{pmatrix} \cos\theta & 0 & -\sin\theta \\ 0 & 1 & 0 \\ \sin\theta & 0 & \cos\theta \end{pmatrix}. \quad (\text{A4})$$

Thus, in the laboratory coordinates, the external stress tensor is $\mathbf{T}^{\text{ext}} = R\mathbf{T}^{\text{ext}'}R^T$. Not much is known about the local values of the ion-induced stress across the fluidized layer; a simple approximation is to consider a constant value for the derivative of τ along the ion beam direction [24]. As noted in Sec. II, remarkably very recent MD simulations [48] of Ar^+ irradiation of Si for $E = 30$ eV (under which the sputtering yield is negligible [31]) seem actually consistent with such a simple variation for τ . At any rate, working in the laboratory reference frame and within our assumptions, the contribution of the external stress to the Stokes equation reduces to

$$\nabla \cdot \mathbf{T}^{\text{ext}} = \nabla' \cdot R^T R \mathbf{T}^{\text{ext}'} R^T = (2G_b \sin\theta, 0, -2G_b \cos\theta), \quad (\text{A5})$$

where we have defined

$$G_b \equiv \left. \frac{d\tau(z')}{dz'} \right|_{z'=h},$$

assumed to be a thickness-independent constant.

The incompressibility and momentum transport relations, Eqs. (A1) and (A2), provide four equations for the pressure and the velocity components in the fluid bulk; in order to have a complete description they should be supplemented with boundary conditions at the top free surface, located at $z = h(x, y, t)$, and at the amorphous-crystalline surface, located at $z = 0$, see Fig. 1(a). For simplicity, we will consider a planar interface with no-slip and no-penetration conditions. Thus, at the bottom boundary, we have $\mathbf{v}(x, y, 0, t) = \mathbf{0}$. At the free surface, the stress balance reads

$$\mathbf{T} \cdot \hat{\mathbf{n}} - 2\sigma\kappa\hat{\mathbf{n}} = \mathbf{0}, \quad (\text{A6})$$

where σ is the surface tension, κ is the mean curvature, and $\hat{\mathbf{n}}$ is the unit normal vector. Taking the scalar product of Eq. (A6) with the normal and tangent vectors $\hat{\mathbf{t}}_1$ and $\hat{\mathbf{t}}_2$ (see Appendix B for the explicit dependence of κ , $\hat{\mathbf{n}}$, $\hat{\mathbf{t}}_1$, and $\hat{\mathbf{t}}_2$ with the partial derivatives of h), we obtain three scalar equations. These equations connect the pressure and velocity components at the free surface with the local surface geometry there. In addition, a so-called kinematic boundary condition is imposed also at the free surface, whereby the time evolution of the latter is exclusively due to fluid motion, namely, [36]

$$\left. \frac{Dz}{Dt} \right|_{z=h} = w(x, y, h, t), \quad (\text{A7})$$

which, using subscripts to denote the partial derivatives, reads

$$h_t = -u(x, y, h)h_x - v(x, y, h)h_y + w(x, y, h). \quad (\text{A8})$$

In principle, we could try to integrate the previous system of equations to obtain the temporal evolution of the pressure and velocity fields. However, due to the disordered spatio-temporal evolution that typically characterizes this type of systems and their fluctuating domains, this task is not easy. Here we follow an alternative methodology based on a gradient expansion similar to the classic long-wave theory of falling films for low flow rates [4,36]. This will lead to a closed evolution equation for the film thickness $h(x, y, t)$ and will allow us to obtain the solution for the remaining variables in terms of this field. Thus, instead of a system of coupled partial differential equations, we will be able to describe this

system using a single scalar evolution equation for the local fluid thickness.

Based on experimental results, a characteristic length, much larger than the average film thickness, is expected to be amplified. This has been predicted by the linear stability analysis of the planar solution for this type of systems [24,44–46], for which the characteristic unstable wavelength is proportional to $\sigma^{1/2}$. In the following, we will consider a dimensionless small parameter ϵ , defined through $\sigma = \alpha\epsilon^{-2}$, where α is a proportionality constant. Hence, the occurrence of a large characteristic length scale in the system (of the order of ϵ^{-1}) makes it natural to introduce “slow” spatial variables on the target plane, $X = \epsilon x$ and $Y = \epsilon y$, and a “slow” time associated with the propagation of the characteristic scale, $T = \epsilon t$ [37,49].

We will construct the solution to the fluid flow problem in the form of a series in powers of ϵ , as $p = \sum_{n=0}^{\infty} \epsilon^n p_n(X, Y, z)$ and $\mathbf{v} = \sum_{n=0}^{\infty} \epsilon^n \mathbf{v}_n(X, Y, z)$. It should be noted that time does not appear explicitly in the expansion of p and \mathbf{v} since these fields are adiabatically slaved to the shape of the free interface, h . Namely, the pressure and the velocity evolve in a timescale which is much faster than the one associated with non-negligible variations in the film thickness. This is a consequence of the slow relaxation time of the system that motivates the neglect of inertial terms in comparison to viscous forces [36].

Thus, substituting the power-series expansion of p and \mathbf{v} in Eqs. (A1) and (A2), we obtain the following system at zeroth order in ϵ :

$$\mu \frac{\partial^2 u_0}{\partial z^2} + 2G_b \sin(\theta) = 0, \quad (\text{A9})$$

$$\mu \frac{\partial^2 v_0}{\partial z^2} = 0, \quad (\text{A10})$$

$$-\frac{\partial p_0}{\partial z} + 2\mu \frac{\partial^2 w_0}{\partial z^2} - 2G_b \cos(\theta) = 0, \quad (\text{A11})$$

$$\frac{\partial w_0}{\partial z} = 0. \quad (\text{A12})$$

The no-slip boundary condition at the bottom interface reads $\mathbf{v}_0(X, Y, 0) = \mathbf{0}$, and the stress balance at the free surface ($z = h$) reduces to

$$0 = \mu \frac{\partial u_0}{\partial z} \Big|_{z=h} - \frac{3}{2} G_s \sin(2\theta), \quad (\text{A13})$$

$$0 = \mu \frac{\partial v_0}{\partial z} \Big|_{z=h}, \quad (\text{A14})$$

$$0 = 2\mu \frac{\partial w_0}{\partial z} \Big|_{z=h} - p_0(X, Y, h) + \frac{3}{2} G_s \left(\cos(2\theta) + \frac{1}{3} \right) - \alpha \frac{\partial^2 h}{\partial X^2} - \alpha \frac{\partial^2 h}{\partial Y^2}, \quad (\text{A15})$$

where

$$G_s \equiv -\tau(z = h). \quad (\text{A16})$$

The solution of Eqs. (A9)–(A15) for the pressure and the streamwise velocity component are, respectively, linear and parabolic profiles in terms of the vertical coordinate. The

spanwise and cross-stream components of the velocity field are $v_0 = w_0 = 0$. Specifically, p_0 and u_0 read

$$p_0 = 3G_s \cos^2(\theta) - G_s + 2G_b(h - z) \cos(\theta) - \alpha \frac{\partial^2 h}{\partial X^2} - \alpha \frac{\partial^2 h}{\partial Y^2}, \quad (\text{A17})$$

$$u_0 = \frac{1}{2\mu} [3G_s \sin(2\theta)z - 2G_b \sin(\theta)(2hz - z^2)]. \quad (\text{A18})$$

Hence, we see that a negative value of τ at the free surface $z = h$ (i.e. $G_s > 0$), increases the pressure locally there. For example, for normal incidence ($\theta = 0^\circ$) on a flat surface, $p_0 = 2G_s$. In general this pressure value also depends on the local curvatures of the free surface and tends to decrease (increase) for convex (concave) surfaces.

At first order in our ϵ expansion, the bulk equations reduce to

$$\mu \frac{\partial^2 u_1}{\partial z^2} + \alpha \frac{\partial^3 h}{\partial X^3} + \alpha \frac{\partial^3 h}{\partial Y^2 \partial X} - 2G_b \cos(\theta) \frac{\partial h}{\partial X} = 0,$$

$$\mu \frac{\partial^2 v_1}{\partial z^2} + \alpha \frac{\partial^3 h}{\partial X^3} + \alpha \frac{\partial^3 h}{\partial Y^2 \partial X} - 2G_b \cos(\theta) \frac{\partial h}{\partial X} = 0,$$

$$-\frac{\partial p_1}{\partial z} + 2\mu \frac{\partial^2 w_1}{\partial z^2} + 2G_b \sin(\theta) \frac{\partial h}{\partial X} = 0,$$

$$\mu \frac{\partial w_1}{\partial z} + 2G_b \sin(\theta) \frac{\partial h}{\partial X} z = 0,$$

with the boundary conditions $\mathbf{v}_1(X, Y, 0) = \mathbf{0}$ and

$$\mu \frac{\partial u_1}{\partial z} \Big|_{z=h} + 3G_s \cos(2\theta) \frac{\partial h}{\partial X} = 0,$$

$$\mu \frac{\partial v_1}{\partial z} \Big|_{z=h} + 3G_s \cos^2(\theta) \frac{\partial h}{\partial Y} = 0,$$

$$2\mu \frac{\partial w_1}{\partial z} \Big|_{z=h} - p_1(X, Y, h) = 0.$$

The solution at this order is

$$p_1 = -2G_b \sin(\theta)(h + z) \frac{\partial h}{\partial X}, \quad (\text{A19})$$

$$u_1 = -\frac{z}{\mu} \left[3G_s \cos(2\theta) + G_b \cos(\theta)(2h - z) \frac{\partial h}{\partial X} - \alpha \left(h - \frac{z}{2} \right) \left(\frac{\partial^3 h}{\partial X^3} + \frac{\partial^3 h}{\partial Y^2 \partial X} \right) \right], \quad (\text{A20})$$

$$v_1 = -\frac{z}{\mu} \left[3G_s \cos^2(\theta) + G_b \cos(\theta)(2h - z) \frac{\partial h}{\partial Y} - \alpha \left(h - \frac{z}{2} \right) \left(\frac{\partial^3 h}{\partial Y^3} + \frac{\partial^3 h}{\partial X^2 \partial Y} \right) \right], \quad (\text{A21})$$

$$w_1 = -\frac{z^2}{\mu} G_b \sin(\theta) \frac{\partial h}{\partial X}. \quad (\text{A22})$$

Note that, as anticipated, the temporal dependence of the pressure and the velocity comes through the evolution of the free interface $h(x, y, t)$.

The previous results allow us to write the solution for p and \mathbf{v} to first order as $p = p_0 + \epsilon p_1$ and $\mathbf{v} = \mathbf{v}_0 + \epsilon \mathbf{v}_1$. However, since the expansion for the incompressibility condition to

order ϵ^2 reads

$$\frac{\partial w_0}{\partial z} + \epsilon \left(\frac{\partial u_0}{\partial X} + \frac{\partial v_0}{\partial Y} + \frac{\partial w_1}{\partial z} \right) + \epsilon^2 \left(\frac{\partial u_1}{\partial X} + \frac{\partial v_1}{\partial Y} + \frac{\partial w_2}{\partial z} \right) = 0, \quad (\text{A23})$$

we still should obtain w_2 to ensure mass conservation for the fluid at the present order. Repeating the previous methodology, we can solve the system equations at order ϵ^2 in the expansion to find p_2 and \mathbf{v}_2 as functions of h and its spatial derivatives. For the vertical velocity component, we obtain

$$\begin{aligned} w_2 = & -\frac{z^2}{2\mu} \left[\left(2G_b \cos(\theta) \left(-h + \frac{z}{3} \right) - 3G_s \cos(2\theta) \right) \frac{\partial^2 h}{\partial X^2} \right. \\ & + \left(2G_b \cos(\theta) \left(-h + \frac{z}{3} \right) - 3G_s \cos^2(\theta) \right) \frac{\partial^2 h}{\partial Y^2} \\ & - 2G_b \cos(\theta) \left(\left(\frac{\partial h}{\partial X} \right)^2 + \left(\frac{\partial h}{\partial Y} \right)^2 \right) \\ & + \alpha \left(h - \frac{z}{3} \right) \left(\frac{\partial^4 h}{\partial X^4} + 2 \frac{\partial^4 h}{\partial Y^2 \partial X^2} + \frac{\partial^4 h}{\partial Y^4} \right) \\ & \left. + \alpha \frac{\partial h}{\partial X} \left(\frac{\partial^3 h}{\partial X^3} + \frac{\partial^3 h}{\partial Y^2 \partial X} \right) + \alpha \frac{\partial h}{\partial Y} \left(\frac{\partial^3 h}{\partial Y^3} + \frac{\partial^3 h}{\partial Y \partial X^2} \right) \right], \end{aligned}$$

which indeed guarantees incompressibility as stated by Eq. (A23).

Rescaling back to the original variables, it is straightforward to obtain the expressions for p and \mathbf{v} as functions of $h(x, y, t)$ and its partial derivatives with respect to x and y . For instance, for the pressure, we obtain

$$\begin{aligned} p = p_0 + \epsilon p_1 = & 3G_s \cos^2(\theta) - G_s + 2G_b(h - z) \cos(\theta) \\ & - \sigma \frac{\partial^2 h}{\partial x^2} - \sigma \frac{\partial^2 h}{\partial y^2} - 2G_b \sin(\theta)(h + z) \frac{\partial h}{\partial x}. \quad (\text{A24}) \end{aligned}$$

If we use the obtained solution for \mathbf{v} in the kinematic condition, Eq. (A8), we finally reach a closed equation for the temporal derivative of h as a function of its spatial derivatives. This equation reads

$$\begin{aligned} h_t = & -a_1 h h_x - a_2 h^2 h_x + b_1 h^2 h_{xx} + 2b_1 h h_x^2 + b_2 h^2 h_{yy} \\ & + 2b_2 h h_y^2 + c h^3 (h_{xx} + h_{yy}) + 3c h^2 (h_x^2 + h_y^2) \\ & - \gamma h^3 (h_{xxx} + 2h_{xxy} + h_{yyy}) \\ & - 3\gamma h^2 [h_x (h_{xxx} + h_{xyy}) + h_y (h_{xxy} + h_{yyy})], \quad (\text{A25}) \end{aligned}$$

with

$$a_1 = \frac{3G_s \sin(2\theta)}{2\mu}, \quad a_2 = \frac{2G_b \sin(\theta)}{\mu}, \quad (\text{A26})$$

$$b_1 = \frac{3G_s \cos(2\theta)}{2\mu}, \quad b_2 = \frac{3G_s \cos^2(\theta)}{2\mu}, \quad (\text{A27})$$

$$c = \frac{2G_b \cos(\theta)}{3\mu}, \quad \gamma = \frac{\sigma}{3\mu}. \quad (\text{A28})$$

Equation (A25) can be written in a more compact form using differential operators, finally becoming Eq. (1) in Sec. II.

An alternative way to obtain Eq. (A25) is by integrating the incompressibility condition across the fluidic layer (from the bottom, $z = 0$, up to the free surface, $z = h$) and using

Leibniz's integral rule. Thus we have

$$\frac{\partial h}{\partial t} = -\frac{\partial}{\partial x} \int_0^h u dz - \frac{\partial}{\partial y} \int_0^h v dz. \quad (\text{A29})$$

Using the solutions for u and v , we get

$$\begin{aligned} \int_0^h u dz = & a_1/2 h^2 + a_2/3 h^3 - b_1 h^2 h_x - c h^3 h_x \\ & + \gamma h^3 (h_{xxx} + h_{xxy}) \equiv J_x, \\ \int_0^h v dz = & -b_2 h^2 h_y - c h^3 h_y + \gamma h^3 (h_{xxy} + h_{yyy}) \equiv J_y, \end{aligned}$$

allowing us to rewrite Eq. (A25) in the conserved form $h_t = -\nabla \cdot \mathbf{J}$, using the current $\mathbf{J} = (J_x, J_y)$.

As indicated in Sec. II, one can perform a weakly nonlinear expansion of Eq. (1) around a uniform-thickness solution h_0 to obtain an evolution equation with lower-order nonlinearities for the perturbation $\tilde{h}(x, y, t)$. This can be particularly appropriate to describe the interface in a regime with waves of small amplitude. Substituting $h(x, y, t) = h_0 + \epsilon \tilde{h}(x, y, t)$ into Eq. (A25) [or in its equivalent form, Eq. (1)], considering the slow spatial scales and expanding up to $\mathcal{O}(\epsilon^4)$, one obtains Eq. (3), which can also be written in a conserved form as $\tilde{h}_t = -\nabla \cdot \tilde{\mathbf{J}}$ with

$$\begin{aligned} \tilde{\mathbf{J}} = & \left(\tilde{a}_1 \tilde{h} + \tilde{a}_2 \tilde{h}^2 + \frac{a_2}{3} \tilde{h}^3, 0 \right) - (h_0^2 \mathbf{B} - c h_0^3 \mathbb{I}) \nabla \tilde{h} \\ & - \tilde{h} \tilde{\mathbf{B}} \nabla \tilde{h} + \gamma h_0^3 \nabla \nabla^2 \tilde{h} + 3\gamma h_0^2 \tilde{h} \nabla \nabla^2 \tilde{h}, \quad (\text{A30}) \end{aligned}$$

where \tilde{a}_1 , \tilde{a}_2 , \mathbf{B} , and $\tilde{\mathbf{B}}$ are defined in Sec. II of the main text.

Finally, let us recall that, much as in the macroscopic problem of a fluid layer flowing down an inclined plane [36], in principle, our continuum model, Eq. (A25), can be systematically improved by considering higher-order terms in our power expansion. This unavoidably also leads to more involved differential equations. For instance, the next order in our present case (to simplify the expression, we just quote the result for one-dimensional substrates) yields the following additional terms on the right-hand side of Eq. (14):

$$-\frac{2}{3\mu} h^2 G_b \sin(\theta) (3h^2 h_{xxx} + 26h h_x h_{xx} + 21h_x^3),$$

which implies a conserved current which includes the additional term

$$J_{\text{higher-order}} = \frac{2}{3\mu} G_b \sin(\theta) \left(\frac{21}{3} h^3 h_x^2 + 3h^4 h_{xx} \right).$$

Sufficiently close to onset of pattern formation, these nonlinear higher-order terms, which in principle induce additional contributions in, e.g., the imaginary part of the linear dispersion relation, are expected to be quantitatively less relevant than their lower-order counterparts [36]. Hence, in the main text we rather focus on the nonlinear dynamics which is already nontrivially described by Eqs. (1) and (14) for 2D and 1D substrates, respectively.

APPENDIX B: EXPLICIT EXPRESSIONS FOR THE MEAN CURVATURE, NORMAL, AND TANGENT VECTORS

For the sake of the reader's convenience, we quote in this Appendix some standard formulas from vector calculus which have been employed in Appendix A. For these and related expressions, see, e.g., Ref. [36].

$$\kappa = \frac{\frac{\partial^2 h}{\partial x^2} (1 + (\frac{\partial h}{\partial y})^2) + \frac{\partial^2 h}{\partial y^2} (1 + (\frac{\partial h}{\partial x})^2) - 2 \frac{\partial h}{\partial x} \frac{\partial h}{\partial y} \frac{\partial^2 h}{\partial y \partial x}}{2(1 + (\frac{\partial h}{\partial x})^2 + (\frac{\partial h}{\partial y})^2)^{3/2}}.$$

$$\hat{\mathbf{n}} = -\frac{\frac{\partial h}{\partial x}}{\sqrt{1 + (\frac{\partial h}{\partial x})^2 + (\frac{\partial h}{\partial y})^2}} \mathbf{e}_x - \frac{\frac{\partial h}{\partial y}}{\sqrt{1 + (\frac{\partial h}{\partial x})^2 + (\frac{\partial h}{\partial y})^2}} \mathbf{e}_y + \frac{1}{\sqrt{1 + (\frac{\partial h}{\partial x})^2 + (\frac{\partial h}{\partial y})^2}} \mathbf{e}_z.$$

$$\hat{\mathbf{t}}_1 = \frac{1}{\sqrt{1 + (\frac{\partial h}{\partial x})^2}} \mathbf{e}_x + \frac{\frac{\partial h}{\partial x}}{\sqrt{1 + (\frac{\partial h}{\partial x})^2}} \mathbf{e}_z.$$

$$\hat{\mathbf{t}}_2 = \frac{1}{\sqrt{1 + (\frac{\partial h}{\partial y})^2}} \mathbf{e}_y + \frac{\frac{\partial h}{\partial y}}{\sqrt{1 + (\frac{\partial h}{\partial y})^2}} \mathbf{e}_z.$$

APPENDIX C: RELEVANT DIMENSIONLESS PARAMETERS

In this Appendix, we show that Eq. (1) depends only on two independent dimensionless parameters (θ and \hat{g}), which allows us to summarize all the relevant information of the

model in the two-dimensional morphological diagram shown in Fig. 1(b).

We can write the height, substrate coordinates, and time in characteristic units as

$$h = \hat{h}_0 \hat{h}, \quad x = \hat{h}_0 \hat{x}, \quad y = \hat{h}_0 \hat{y}, \quad t = \hat{t}_0 \hat{t}, \quad (\text{C1})$$

where $\hat{h}_0 = 2\sigma/(9G_s)$ and $\hat{t}_0 = 2\mu/(3G_s)$ have dimensions of length and time, respectively, and \hat{h} , \hat{x} , \hat{y} , and \hat{t} are dimensionless. Under this transformation, Eq. (1) takes the following dimensionless form:

$$\hat{h}_{\hat{t}} = -\sin(2\theta) \hat{h} \hat{h}_{\hat{x}} - \frac{4}{3} \hat{g} \sin(\theta) \hat{h}^2 \hat{h}_{\hat{x}} + \nabla \cdot (\hat{h}^2 \hat{\mathbf{B}} \nabla \hat{h}) + \frac{4}{9} \hat{g} \nabla \cdot (\hat{h}^3 \nabla \hat{h}) - \nabla \cdot (\hat{h}^3 \nabla \nabla^2 \hat{h}), \quad (\text{C2})$$

where derivative operators are in the rescaled substrate coordinates,

$$\hat{\mathbf{B}} \equiv \begin{bmatrix} \cos(2\theta) & 0 \\ 0 & \cos^2(\theta) \end{bmatrix}, \quad (\text{C3})$$

and $\hat{g} = G_b \hat{h}_0 / G_s$ is the dimensionless stress ratio defined in Eq. (4). Thus out of the five parameters which initially enter Eq. (1), namely, θ , G_s , G_b , μ , and σ , the rescalings made in (C1) yield the differential equation, Eq. (C2), which only depends on the incidence angle θ and one dimensionless combination \hat{g} , whose magnitude and sign determine the full dynamics described by the continuum model. A similar conclusion applies in the case of the weakly nonlinear model, Eq. (3).

-
- [1] R. C. Desai and R. Kapral, *Dynamics of Self-organized and Self-assembled Structures* (Cambridge University Press, Cambridge, England, 2009).
- [2] M. Cross and H. Greenside, *Pattern Formation and Dynamics in Nonequilibrium Systems* (Cambridge University Press, Cambridge, England, 2009).
- [3] C. Misbah, *Complex Dynamics and Morphogenesis* (Springer Science & Business Media, Dordrecht, 2017).
- [4] F. Charru, *Hydrodynamic Instabilities* (Cambridge University Press, Cambridge, England, 2011).
- [5] N. Ghoniem and D. Walgraef, *Instabilities and Self-organization in Materials* (Oxford University Press, Oxford, England, 2008).
- [6] S. Yadavali and R. Kalyanaraman, *AIP Adv.* **4**, 047116 (2014).
- [7] M. C. Giordano and F. B. de Mongeot, *Adv. Mater.* **30**, 1801840 (2018).
- [8] N. Taniguchi, in *Proceedings of the International Conference on Production Engineering* (Japan Society of Precision Engineering, Tokyo, Japan, 1974), pp. 18–23.
- [9] M. A. Nastasi, J. W. Mayer, and J. K. Hirvonen, *Ion-Solid Interactions: Fundamentals and Applications* (Cambridge University Press, New York, 1996).
- [10] J. Muñoz-García, L. Vázquez, R. Cuerno, J. A. Sánchez-García, M. Castro, and R. Gago, in *Toward Functional Nanomaterials*, edited by Z. M. Wang (Springer, New York, 2009), pp. 323–398.
- [11] R. Cunningham, P. Haymann, C. Lecomte, W. Moore, and J. Trillat, *J. Appl. Phys.* **31**, 839 (1960).
- [12] M. Navez, C. Sella, and D. Chaperot, *Comptes Rendus Acad. Sci.* **254**, 240 (1962).
- [13] S. Facsko, T. Dekorsy, C. Koerdt, C. Trappe, H. Kurz, A. Vogt, and H. L. Hartnagel, *Science* **285**, 1551 (1999).
- [14] D. Kan, T. Terashima, R. Kanda, A. Masuno, K. Tanaka, S. Chu, H. Kan, A. Ishizumi, Y. Kanemitsu, Y. Shimakawa *et al.*, *Nat. Mater.* **4**, 816 (2005).
- [15] Y. K. Liao, Y. C. Wang, Y. T. Yen, C. H. Chen, D. H. Hsieh, S. C. Chen, C. Y. Lee, C. C. Lai, W. C. Kuo, J. Y. Juang *et al.*, *ACS Nano* **7**, 7318 (2013).
- [16] O. Azzaroni, M. Fonticelli, G. Benítez, P. Schilardi, R. Gago, I. Caretti, L. Vázquez, and R. Salvarezza, *Adv. Mater.* **16**, 405 (2004).
- [17] P. S. Yang, P. H. Cheng, C. R. Kao, and M. J. Chen, *Sci. Rep.* **6**, 29625 (2016).
- [18] B. Teshome, S. Facsko, and A. Keller, *Nanoscale* **6**, 1790 (2014).
- [19] I. Wittenbrink, A. Hausmann, K. Schickle, I. Lauria, R. Davtalyan, M. Foss, A. Keller, and H. Fischer, *Biomaterials* **62**, 58 (2015).

- [20] Y. T. Yen, Y. C. Wang, Y. Z. Chen, H. W. Tsai, F. Hu, S. M. Lin, Y. J. Chen, C. C. Lai, W. Liu, T. H. Wang *et al.*, *ACS Appl. Mater. Inter.* **6**, 8327 (2014).
- [21] B. Pabón, J. Beltrán, G. Sánchez-Santolino, I. Palacio, J. López-Sánchez, J. Rubio-Zuazo, J. Rojo, P. Ferrer, A. Mascaraque, M. Muñoz *et al.*, *Nat. Commun.* **6**, 6147 (2015).
- [22] H. Gnaser, *Low Energy Ion Irradiation of Solid Surfaces* (Springer-Verlag, Heidelberg, 1999).
- [23] N. A. Krishnan, B. Wang, Y. Le Pape, G. Sant, and M. Bauchy, *J. Chem. Phys.* **146**, 204502 (2017).
- [24] A. Moreno-Barrado, M. Castro, R. Gago, L. Vázquez, J. Muñoz-García, A. Redondo-Cubero, B. Galiana, C. Ballesteros, and R. Cuerno, *Phys. Rev. B* **91**, 155303 (2015).
- [25] J. Muñoz-García, L. Vázquez, M. Castro, R. Gago, A. Redondo-Cubero, A. Moreno-Barrado, and R. Cuerno, *Mater. Sci. Eng. R: Rep.* **86**, 1 (2014).
- [26] R. Cuerno and A.-L. Barabási, *Phys. Rev. Lett.* **74**, 4746 (1995).
- [27] T. C. Kim, C.-M. Ghim, H. J. Kim, D. H. Kim, D. Y. Noh, N. D. Kim, J. W. Chung, J. S. Yang, Y. J. Chang, T. W. Noh *et al.*, *Phys. Rev. Lett.* **94**, 139602 (2005).
- [28] M. Castro, R. Cuerno, L. Vázquez, and R. Gago, *Phys. Rev. Lett.* **94**, 016102 (2005).
- [29] J. Muñoz-García, M. Castro, and R. Cuerno, *Phys. Rev. Lett.* **96**, 086101 (2006).
- [30] M. P. Harrison, D. A. Pearson, and R. M. Bradley, *Phys. Rev. E* **96**, 032804 (2017).
- [31] A. Lopez-Cazalilla, D. Chowdhury, A. Ilinov, S. Mondal, P. Barman, S. Bhattacharyya, D. Ghose, F. Djurabekova, K. Nordlund, and S. Norris, *J. Appl. Phys.* **123**, 235108 (2018).
- [32] S. A. Norris, J. C. Perkinson, M. Mokhtarzadeh, E. Anzenberg, M. J. Aziz, and K. F. Ludwig, *Sci. Rep.* **7**, 2016 (2017).
- [33] L. Bocquet and E. Charlaix, *Chem. Soc. Rev.* **39**, 1073 (2010).
- [34] P. Tabeling, *Introduction to Microfluidics* (Oxford University Press, Oxford, England, 2005).
- [35] C. Kleinstreuer, *Microfluidics and Nanofluidics: Theory and Selected Applications* (Wiley, Hoboken, New Jersey, 2013).
- [36] S. Kalliadasis, C. Ruyer-Quil, B. Scheid, and M. G. Velarde, *Falling Liquid Films* (Springer Science & Business Media, New York, 2011), Vol. 176.
- [37] A. Oron, S. H. Davis, and S. G. Bankoff, *Rev. Mod. Phys.* **69**, 931 (1997).
- [38] C. Christov and M. Velarde, *Physica D* **86**, 323 (1995).
- [39] M. Velarde and A. Nepomnyashchy, in *Dissipative Solitons: From Optics to Biology and Medicine*, edited by A. Ankiewicz and N. Akhmediev (Springer, Berlin, 2008), p. 1.
- [40] M. C. Moore, N. Kalyanasundaram, J. B. Freund, and H. T. Johnson, *Nucl. Instrum. Meth. B* **225**, 241 (2004).
- [41] N. Kalyanasundaram, M. C. Moore, J. B. Freund, and H. T. Johnson, *Acta Mater.* **54**, 483 (2006).
- [42] C. S. Madi, E. Anzenberg, K. F. Ludwig, Jr., and M. J. Aziz, *Phys. Rev. Lett.* **106**, 066101 (2011).
- [43] S. A. Norris, *Phys. Rev. B* **85**, 155325 (2012).
- [44] M. Castro and R. Cuerno, *Appl. Surf. Sci.* **258**, 4171 (2012).
- [45] M. Castro, R. Gago, L. Vázquez, J. Muñoz-García, and R. Cuerno, *Phys. Rev. B* **86**, 214107 (2012).
- [46] S. A. Norris, *Phys. Rev. B* **86**, 235405 (2012).
- [47] A. Moreno-Barrado, R. Gago, A. Redondo-Cubero, L. Vázquez, J. Muñoz-García, R. Cuerno, K. Lorenz, and M. Castro, *EPL* **109**, 48003 (2015).
- [48] A. Lopez-Cazalilla, Ph.D. thesis, University of Helsinki, 2019.
- [49] R. V. Craster and O. K. Matar, *Rev. Mod. Phys.* **81**, 1131 (2009).
- [50] S. E. Orchard, *Appl. Sci. Res. A* **11**, 451 (1962).
- [51] A. L. Bertozzi, A. Münch, X. Fanton, and A. M. Cazabat, *Phys. Rev. Lett.* **81**, 5169 (1998).
- [52] M. Bowen, J. Sur, A. L. Bertozzi, and R. P. Behringer, *Physica D* **209**, 36 (2005).
- [53] A. Nepomnyashchy, in *Fluid Dynamics at Interfaces*, edited by W. Shyy and R. Narayanan (Cambridge University Press, Cambridge, England, 1999), pp. 85–98.
- [54] C. C. Umbach, R. L. Headrick, and K.-C. Chang, *Phys. Rev. Lett.* **87**, 246104 (2001).
- [55] A. Moreno-Barrado, M. Castro, J. Muñoz-García, and R. Cuerno, *Nucl. Inst. Methods Phys. Res. B* **365**, 13 (2015).
- [56] C. S. Madi, B. Davidovitch, H. B. George, S. A. Norris, M. P. Brenner, and M. J. Aziz, *Phys. Rev. Lett.* **101**, 246102 (2008).
- [57] G. Carter and V. Vishnyakov, *Phys. Rev. B* **54**, 17647 (1996).
- [58] R. M. Bradley and J. M. E. Harper, *J. Vac. Sci. Technol. A* **6**, 2390 (1988).
- [59] P. M. Chaikin and T. C. Lubensky, *Principles of Condensed Matter Physics* (Cambridge University Press, Cambridge, England, 1995).
- [60] R. M. M. Mattheij, S. W. Rienstra, and J. H. P. ten Thije Boonkkamp, *Partial Differential Equations: Modeling, Analysis, Computation* (SIAM, Philadelphia, 2005).
- [61] S. Habenicht, K. P. Lieb, J. Koch, and A. D. Wieck, *Phys. Rev. B* **65**, 115327 (2002).
- [62] P. F. A. Alkemade, *Phys. Rev. Lett.* **96**, 107602 (2006).
- [63] H. Hofsäss, K. Zhang, H. G. Gehrke, and C. Brüsewitz, *Phys. Rev. B* **88**, 075426 (2013).
- [64] D. Kramczynski, B. Reuscher, and H. Gnaser, *Phys. Rev. B* **89**, 205422 (2014).
- [65] See Supplemental Material at <http://link.aps.org/supplemental/10.1103/PhysRevB.100.205421> for 1D and 2D movies produced through the numerical simulations described in the main text.
- [66] H. Gnaser, B. Reuscher, and A. Zeuner, *Nucl. Instrum. Meth. B* **285**, 142 (2012).
- [67] Q. Wei, J. Lian, L. A. Boatner, L. Wang, and R. C. Ewing, *Phys. Rev. B* **80**, 085413 (2009).
- [68] H. Hofsäss, O. Bobes, and K. Zhang, *AIP Conf. Proc.* **1525**, 386 (2013).
- [69] W. L. Chan and E. Chason, *J. Appl. Phys.* **101**, 121301 (2007).
- [70] G. B. Whitham, *Linear and Nonlinear Waves* (Wiley, New York, 1974).
- [71] A. L. Bertozzi and M. Shearer, *SIAM J. Math. Anal.* **32**, 194 (2003).
- [72] A. L. Bertozzi, A. Münch, and M. Shearer, *Physica D* **134**, 431 (1999).
- [73] H. H. Chen, O. A. Urquidez, S. Ichim, L. H. Rodriguez, M. P. Brenner, and M. J. Aziz, *Science* **310**, 294 (2005).
- [74] M. Holmes-Cerfon, M. J. Aziz, and M. P. Brenner, *Phys. Rev. B* **85**, 165441 (2012).
- [75] M. Holmes-Cerfon, W. Zhou, A. L. Bertozzi, M. P. Brenner, and M. J. Aziz, *Appl. Phys. Lett.* **101**, 143109 (2012).
- [76] D. A. Pearson and R. M. Bradley, *J. Phys.: Condens. Mat.* **27**, 015010 (2015).

- [77] J. C. Perkinson, M. J. Aziz, M. P. Brenner, and M. C. Holmes-Cerfon, *Proc. Natl. Acad. Sci.* **113**, 11425 (2016).
- [78] C. Misbah, O. Pierre-Louis, and Y. Saito, *Rev. Mod. Phys.* **82**, 981 (2010).
- [79] P. Klapetek and D. Nečas, *Open Phys.* **10**, 181 (2012).
- [80] C. S. Madi, H. B. George, and M. Aziz, *J. Phys.: Condens. Mat.* **21**, 224010 (2009).
- [81] A. Redondo-Cubero, R. Gago, F. J. Palomares, A. Mücklich, M. Vinnichenko, and L. Vázquez, *Phys. Rev. B* **86**, 085436 (2012).
- [82] E. Anzenberg, J. C. Perkinson, C. S. Madi, M. J. Aziz, and K. F. Ludwig Jr, *Phys. Rev. B* **86**, 245412 (2012).
- [83] M. Teichmann, J. Lorbeer, B. Ziberi, F. Frost, and B. Rauschenbach, *New J. Phys.* **15**, 103029 (2013).
- [84] R. M. Bradley and H. Hofsäss, *J. Appl. Phys.* **116**, 234304 (2014).
- [85] R. M. Bradley and H. Hofsäss, *J. Appl. Phys.* **120**, 074302 (2016).
- [86] E. A. Demekhin, E. N. Kalaidin, S. Kalliadasis, and S. Y. Vlaskin, *Phys. Rev. E* **82**, 036322 (2010).